



Review

Recent Advances in Two-Dimensional Transition Metal Dichalcogenide Nanocomposites Biosensors for Virus Detection before and during COVID-19 Outbreak

Ching Ying Katherine Lam ^{1,†} , Qin Zhang ^{1,†}, Bohan Yin ¹, Yingying Huang ¹, Hui Wang ², Mo Yang ^{1,*} and Siu Hong Dexter Wong ^{1,*}

- ¹ Department of Biomedical Engineering, Hong Kong Polytechnic University, Hong Kong 999077, China; katherine009.lam@connect.polyu.hk (C.Y.K.L.); zhangqin.zhang@connect.polyu.hk (Q.Z.); bohan.yin@polyu.edu.hk (B.Y.); daisy-y.huang@polyu.edu.hk (Y.H.)
- ² Fishery Resource and Environment Research Center, Chinese Academy of Fishery Sciences, Beijing 100141, China; wanghui@cafs.ac.cn
- * Correspondence: mo.yang@polyu.edu.hk (M.Y.); shongwong@polyu.edu.hk (S.H.D.W.); Tel.: +852-2766-4946 (M.Y.); +852-2766-7676 (S.H.D.W.)
- † These authors contributed equally to this work.

Abstract: The deadly Severe Acute Respiratory Syndrome Coronavirus 2 (SARS-CoV-2) outbreak has become one of the most challenging pandemics in the last century. Clinical diagnosis reports a high infection rate within a large population and a rapid mutation rate upon every individual infection. The polymerase chain reaction has been a powerful and gold standard molecular diagnostic technique over the past few decades and hence a promising tool to detect the SARS-CoV-2 nucleic acid sequences. However, it can be costly and involved in complicated processes with a high demand for on-site tests. This pandemic emphasizes the critical need for designing cost-effective and fast diagnosis strategies to prevent a potential viral source by ultrasensitive and selective biosensors. Two-dimensional (2D) transition metal dichalcogenide (TMD) nanocomposites have been developed with unique physical and chemical properties crucial for building up nucleic acid and protein biosensors. In this review, we cover various types of 2D TMD biosensors available for virus detection via the mechanisms of photoluminescence/optical, field-effect transistor, surface plasmon resonance, and electrochemical signals. We summarize the current state-of-the-art applications of 2D TMD nanocomposite systems for sensing proteins/nucleic acid from different types of lethal viruses. Finally, we identify and discuss the advantages and limitations of TMD-based nanocomposites biosensors for viral recognition.

Keywords: transition metal dichalcogenide; nanocomposites; SARS-CoV-2; biosensors



Citation: Lam, C.Y.K.; Zhang, Q.; Yin, B.; Huang, Y.; Wang, H.; Yang, M.; Wong, S.H.D. Recent Advances in Two-Dimensional Transition Metal Dichalcogenide Nanocomposites Biosensors for Virus Detection before and during COVID-19 Outbreak. *J. Compos. Sci.* **2021**, *5*, 190. <https://doi.org/10.3390/jcs5070190>

Academic Editor:
Francesco Tornabene

Received: 6 July 2021
Accepted: 15 July 2021
Published: 18 July 2021

Publisher's Note: MDPI stays neutral with regard to jurisdictional claims in published maps and institutional affiliations.



Copyright: © 2021 by the authors. Licensee MDPI, Basel, Switzerland. This article is an open access article distributed under the terms and conditions of the Creative Commons Attribution (CC BY) license (<https://creativecommons.org/licenses/by/4.0/>).

1. Introduction

1.1. Origin and Discovery of Viruses

In 1892, a Russian botanist, Dmitri Ivanovsky, discovered a non-bacterial pathogen infecting tobacco plants [1]. This pathogen was later confirmed to be the tobacco mosaic virus by a microbiologist, Martinus Beijerinck, in 1898 [2]. Nowadays, over 6000 virus species have been discovered with extremely small in size (~20–400 nm), and the viruses can only be observed employing electron microscopy. The origins of viruses in the evolutionary history of life are unclear. It has been postulated that the viruses acquired the ancient structures preceding the divergence of life forms into Bacteria, Archaea, and Eukarya [3].

Viruses exist in the form of independent particles with no metabolic activities and consist of (i) genetic materials, including long molecules single- or double-stranded DNA (ssDNA or dsDNA), or single stranded-RNA (ssRNA) that encode the structural components, (ii) protein coats (capsid) and in some cases (iii) outer envelope of lipids [4]. The virus particle morphology ranges from helical, icosahedral, spherical, and even more

complex structures, which may imply the potential viral behaviour and function [5]. Once a virus infects a host cell, the virus adopts a mechanism to force the host cell to replicate thousands of identical copies of the original virus, leading to the death of the host cell by cytopathic effects [6]. This cycle will be repeated after the replicated viruses infecting new host cells unless triggering adequate immune cells (adaptive immune system) to encounter the pathogens. Thus far, viruses can be harmful and potentially lethal to humans.

1.2. The Pandemic

In 1960, coronavirus was first identified to be a family of enveloped, single-stranded, positive-sense, and highly diverse RNA viruses, including human coronavirus HKU1 (hCoV-HKU1), hCoV-OC43, hCoV-NL63, and hCoV-229E [7]. They were gradually recognized as a cause of common cold (5–30%), leading to mild and non-fatal symptoms in humans [8]. However, in 2002, the coronavirus acquired a mutated form that caused the outbreak of severe acute respiratory syndrome (SARS), mainly identified in Guangdong-related regions and Hong Kong, China, and 28 different countries and territories [9]. This outbreak caused over 8000 infections and at least 774 deaths worldwide from 2002 to 2004 (~10% death rate) [10]. In 2012, a similar form of coronavirus causing Middle East respiratory syndrome (MERS) was first identified, and most infected cases occurred in Arabian Peninsula [11]. Large outbreaks of MERS also occurred in Southern Korea in 2015 and in Saudi Arabia in 2018. Although the MERS outbreak is not frequently occurred, it has never ended despite the pandemic scale. Until March 2021, the total confirmed cases were 2574, but the death number was 885 (~34% death rate) [12]. Unfortunately, an exceptionally huge pandemic—coronavirus disease 2019 (COVID-19) has been caused by severe acute respiratory syndrome coronavirus 2 (SARS-CoV-2) in late 2019 and was initially discovered in Wuhan, China, and swiftly spread across the world [13]. It is described as a successor to SARS-CoV-1 (SARS outbreak in 2002–2004) and has caused more than 113 million COVID-19 confirmed cases, including 2.5 million deaths worldwide (~2% death rate) documented in February 2021 [13]. Such pandemic is still ongoing, and SARS-CoV-2 remains highly infectious through different transmissions due to the mutation-mediated adaptation for infection of the intermediated civet host as well as interhuman transmission [14]. Hence, medical personnel and researchers have been inventing different solutions to fight against pandemics nowadays. Also, many countries have adopted a lockdown policy to prevent disease outbreaks. Thus far, such pandemic has been negatively influencing both worldwide public health and the economy. Although several currently available SARS-CoV-2 vaccines show protective efficacy, they may not address the rapid viral mutation rate concerns because the efficacy of the antibody responses induced by the original strain against the mutation strain is questionable [15]. Therefore, the current cost-effective method for minimizing the pandemics is to utilize promising diagnostic tools to screen out the infected patients to isolate another potential viral source and prevent the outbreak.

Despite the aforementioned three documented highly pathogenic and lethal hCoVs, other chronic/life-threatening human diseases such as hepatitis and cancers caused by hepatitis B and C virus [16], acquired immunodeficiency syndromes (AIDS) caused by human immunodeficiency viruses (HIV) [17], Zika fever caused by Zika virus (ZIKV) [18], and deadly Ebola virus disease (EVD) caused by Ebola viruses [19] remain a significant challenge to human life every year. More importantly, infected people serve as the main pathogen carriers for spreading the virus in large populations. The development of particular viral vaccines remains high cost (unprecedented research efforts), time-consuming (vast scale clinical trials to address safety concerns), and substantial challenge (efficacy) [7]. Hence, cost-effective and robust biosensors are highly desirable for the rapid detection of viral infection in patients for early treatment and preventive strategies.

1.3. Conventional Diagnostic Tools on Viral Protein- and Nucleic Acid-Based Biomarkers

Clinically available diagnostic methods for detection of virus and viral diseases by the techniques of (1) cell culture (infectivity assay) [20], (2) hemagglutination assay (viral

protein revelation) [21], (3) electron microscopy (viral morphology) [22], (4) enzyme-linked immunosorbent assay (ELISA, antibody-based protein detection) [23], and (5) polymerase chain reaction (PCR, nucleic acid-based detection) [24]. Techniques (1) to (3) are low cost and allow broad-spectrum detection, but (1) it is hard to maintain a good culture status in a long incubation period, and susceptible to contamination; (2) and (3) have low sensitivity. (4) has much variety and offers high specificity (specific IgM and IgA antibody) and sensitivity (cut-off concentration: 50 ng mL⁻¹ or 5 IU mL⁻¹), but such sensitivity is dependent on the host antibody response upon infection. (5) has the highest sensitivity (complementary DNA hybridization) towards nucleic acids as one single copy of DNA can be amplified to one billion copies (limit of detection (LOD): 100 copies mL⁻¹). However, PCR is also extremely liable for contamination and requires a highly skilled operator to control sophisticated instruments. Despite the limitations, these techniques remain the standard virus detection methods, especially (4) and (5) regarding gold standard methods to detect viral proteins and nucleic acids, respectively, for clinical diagnosis.

1.3.1. Cell Culture-Based Virus Diagnosis

In 1913, Steinhardt and colleagues successfully cultivated a virus known as vaccinia on the skin of rabbits, of which the infected tissue was harvested into tubes of ascitic broth at 37 °C for continuous culture up to 12 days [25]. Subsequently, they transferred the virus to other tissues, such as the cornea of rabbits (symptom: ulcers) and a calfskin (symptom: scattered pustules). The virus remained active for over a month, indicating a good incubation condition for the virus. Nowadays, researchers have been adopting a method that a monolayer of a selected cell line can be grown on the side of a standard container, a screw-cap tube glass (16 mm × 125 mm) with the virus-containing cell culture media and antibiotics to prevent bacteria growth [20]. The selection of a specific cell line can identify viruses accurately. The cell lines typically are rhesus monkey kidney cells (RhMK), human foreskin fibroblasts, A549, primary rabbit kidney cells, and MRC-5.

A standard protocol is employed to estimate the proliferation of the virus in the cells by observing the cell morphological changes (e.g., swelling, shrinking, and syncytium formation), defined as cytopathic effect (CPE), indicating the presence of the virus. However, the time required for the appearance of CPE can be subject to the virus type, commonly 5–10 days for most cases and 24 h for herpes simplex virus (HSV). On the other hand, immunofluorescence (IF) diagnosis can be performed to identify viral-infected cells via monoclonal antibodies against a specific virus, and subsequently, the monoclonal antibodies are sandwiched with fluorescently labeled secondary anti-species antibodies. This identification method provides a high sensitivity of detecting viruses, such as 93.8% for adenovirus, 88.9% for cytomegalovirus (CMV), and 100% for HSV [26]. However, it is not possible to detect all viruses, such as serotypes in the enterovirus family that showed cross-reaction between monoclonal antibodies and the enteroviral serotypes [27]. Moreover, cell culture-based virus diagnosis can be costly due to the purchase and maintenance of monolayer cells. Nevertheless, cell culture is considered the gold standard for virus isolation and identification [28].

1.3.2. Hemagglutination Assay

The hemagglutination assay (HA) and the hemagglutination inhibition assay (HI) were developed in 1942 by a virologist, George Hirst, to determine the relative concentration of influenza virus and antibodies employing red blood cell (RBCs) agglutination. [29] The underlying mechanism utilizes N-acetylneuraminic acid-containing receptors of RBCs surface binding to the hemagglutinin glycoprotein of the influenza virus surface to form an agglutinated lattice structure of RBCs and virus particles. Specific pathogen-free chicken erythrocytes are selected because of their fast settling time and clear settling pattern compared to other species. The lattice can maintain RBCs suspended distributed in water that appears as a reddish solution. In contrast, RBCs sink to the bottom of the well if the virus concentration is too low as little lattice is formed to glue RBCs as a suspended form.

This method can determine the relative concentration of viruses and also bacterial species, such as vibrios and staphylococci [30]. Therefore, HA is not an identification assay.

HA can be accompanied by HI to analyze the type and/or subtype of viruses antigenically [31]. Basically, the HI test involves antibodies, influenza viruses, and RBCs mixed in the wells of a microtiter plate. The antibodies are isolated from a specific flu virus infecting an animal that is originally immunologically naïve. This animal creates antibodies that are able to bind to the antigen of the specific virus surface. Therefore, the HI test measures the affinity between the known antibodies and the unknown viruses from a sample. With strong affinity, the incubated antibodies can recognize and bind to the incubated virus and hence inhibit RBCs from hemagglutination. Thus far, the RBCs sink to the bottom, and a red dot can be observed. Otherwise, the RBCs remain suspended in the solution in case of low affinity between the antibodies and the virus. Overall, the assays are simple and inexpensive [32]. The instruments and reagents are generally accessible by the common laboratory. The assay can provide results within a few hours. Receptor-destroying enzymes may be added to the samples to prevent non-specific inhibition [33]. However, the assay requires optimization of incubation times, RBCs concentration, and RBC type for obtaining reliable results, which are subjective to the individual and the agreement between readers that may make inconsistency [34].

1.3.3. Electron Microscopy

Electron microscopy (EM), typically transmission or scanning EM (TEM or SEM), offers a high resolution, unbiased and rapid method to visualize virus-like particles from clinical specimens, cell culture fluids, and tissue samples at the nanoscale [22]. TEM has been a front line in the surveillance of viruses that can detect biological threats, especially during current pandemics [35]. Generally, the fluid needs to be dried on a small and thin metal grid (~3 mm diameter) for the observation under TEM. Scientists undertake negative staining to enhance the structural contrast of the viruses. To obtain a successful visualization, EM requires the virus concentration from a sample with 10^5 to 10^6 virus particles per mL. However, such high viral concentration may require a high blood load for viruses such as hepatitis B, Ebola, HSV, and other vesicular fluid containing poxvirus. Moreover, it is hard to distinguish different viruses with similar morphology. Several methods, such as ultracentrifugation, ultrafiltration, or agar diffusion, can improve the viral purity before performing TEM [36]. Besides, immunoelectron microscopy is another strategy to improve EM low viral concentration sensitivity by adding specific antibodies to cluster viruses into larger particles for easy recognition [37]. Scientists also employ immunogold-labelling to reveal the position of virus components via incubating viral-specific antibodies that are subsequently bound by the secondary antibodies labelled gold nanoparticles [38]. Despite the recent advances in EM technology to detect viruses, several limitations are concerned. For instance, cell organelles and artifacts can be mistaken for viruses. Improper shipment process or preservation can distort viruses and cellular organelles. Hence, sample preparation is critical towards preserving recognizable viruses.

1.3.4. Enzyme-Linked Immunosorbent Assay (ELISA)-Based Detection

An ELISA employs a microplate-based assay technique for detecting and quantifying proteins (antigen), antibodies, and hormones, which are immobilized as solid-phase and bonded with specific antibodies from a liquid phase. The bonded antibodies carrying detection reagents (e.g., HRP, horseradish peroxidase) can generate detection signals (optical light absorbance at a specific wavelength) using particular enzymes (e.g., OPD, o-phenylenediamine dihydrochloride) [39]. Thus, the signals intensity corresponding to the concentration of the analyte can be measured by an ELISA plate reader. There are many types of ELISA tests, including direct ELISA, sandwich ELISA, competitive ELISA, and reverse ELISA, but their working mechanisms remain similar. Sandwich ELISA is 2–5 times more sensitive than direct or indirect ELISA and high specificity because of the usage of two antibodies (one immobilized antibody for capturing the antigen and one

detection antibody conjugated to a detection reagent for binding the captured antigen) for recognizing different epitopes of one antigen. Hence, it is the most popular ELISA method.

To detect SARS-CoV-2, the extraction and identification of the proteins are necessary. Typically, SARS-CoV-2 contains four known structural proteins: surface spike protein (S protein with two subunits, S1 and S2 forming homotrimers) for viral entry into the host cells by binding to angiotensin-converting enzyme 2 (ACE2), the small envelope (E) glycoprotein for the production and maturation of the virus, membrane (M) glycoprotein for stabilizing the complex between nucleocapsid (N) protein and virus RNA, and N protein for regulating replication cycle of virus RNA and the response of the infected cells (Figure 1a) [40]. S and N proteins are the most popular biomarkers and potential vaccine targets of SARS-CoV-2 due to their high concentration and corresponding roles [41]. To support the development of rapid diagnostic tools, recombinant S and N antigens and antibodies have been manufactured as the positive controls and detection reagents, respectively (Table 1). There are several commercially available kit products for probing, mainly S protein, such as REGN-COV2, 47D11, and AbEpic, although they have not been approved by the U.S. Food and Drug Administration (FDA). On the other hand, the presence of antibodies against S and N protein in blood from patients can also be an indicator of positive infection, and hence ELISA is also available to detect specific IgM/IgG antibodies in human serum, plasma, or whole blood [42]. It has been suggested that specific IgM against the viral protein can be detected within 3–7 days after the onset of infections. Nevertheless, ELISA procedures can be challenging to optimize, and require intensive labour work and sophisticated techniques. The consumption of two types of antibodies in sandwich ELISA also increases the cost for each assay.

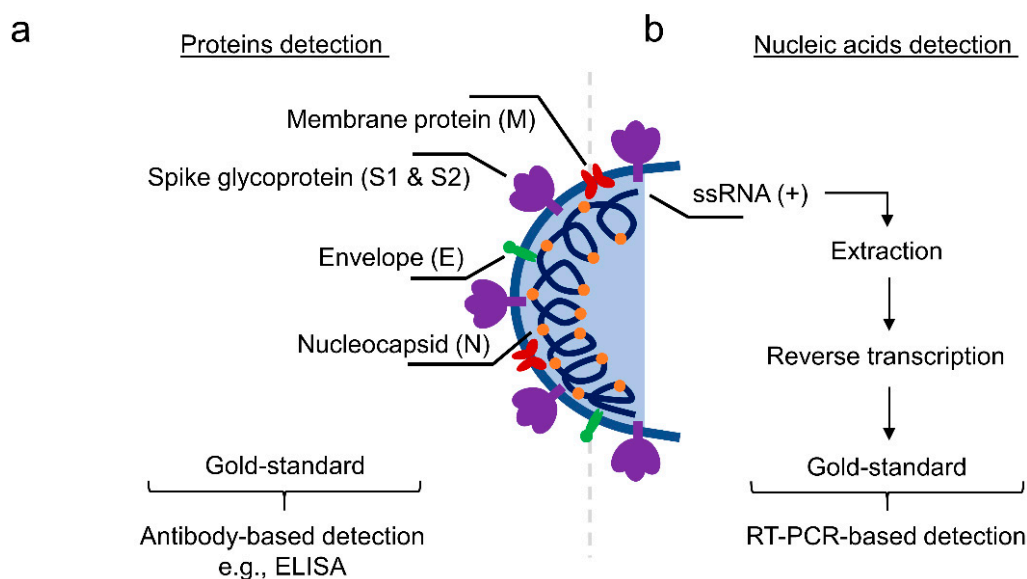


Figure 1. Schematic illustration of structural components of SARS-CoV-2. (a) Protein-based biomarkers for viral detection. (b) Nucleic acids-based biomarkers for viral detection.

1.3.5. PCR-Based Detection

During the outbreak of COVID-19, RT-PCR or quantitative PCR (qPCR) is the primarily used molecular biology technique to detect the potential infection of patients in hospitals [43]. Generally, before PCR, the handling procedure involves RNA isolation and reverse transcription of the RNA into cDNA for better stability (Figure 1b). Subsequently, PCR is performed by mixing a set concentration of the buffer to maintain pH, dNTPs as the source of nucleotides, primers of the target gene, cDNA as the template, Taq polymerase for DNA replication, and SYBR green dye for binding and quantifying double-strand DNA (dsDNA). The mixture undergoes a series of temperature variation cycles for denaturation,

annealing, and elongation and ultimately turns the results into cycle threshold (Ct) values. The relative expression level of the target gene is calculated by comparing the Ct values of control and experimental samples. After the outbreak of COVID-19, World Health Organization (WHO) published a standard protocol of RT-PCR for detecting SARS-CoV-2 on 14 January 2020 [43]. Therefore, PCR has been playing an important role during the pandemic era. More importantly, we have to understand the overall SARS-CoV-2 genome to identify the target sequence. Many laboratories have sequenced the genomes and shared them on Global Initiative on Sharing All Influenza Data (GISAID) database [44]. The revealed genome consists of open read frames (ORFs) 1ab (two-thirds) for encoding 16 non-structural proteins, four structural proteins (S, M, E, and N), and at least six accessory proteins (3a, 6, 7a, 7b, 8 and maybe 9–10) as the whole genome (Figure 2). Theoretically, we can design any pair of primers targeting a specific sequence from the viral genome (Table 2) [45–48]. The reports of targeting M protein and ORF6-8 have been rare.

Table 1. Summary of commercially available SARS-CoV-2 related S and N recombinant antigen and antibody production for ELISA assays. Source: <https://www.nordicbiosite.com/news/sars-cov-2--2019-ncov-detection-antibodies-and-antigens> (Accessed: 20 April 2021).

Protein Name	Product Name	Cat. No.	Antigens/Antibodies
N-protein	SARS-CoV-2 (2019-nCoV) Nucleocapsid Protein (His tag)	40588-V08B	Antigens
S-protein	SARS-CoV-2 (2019-nCoV) Spike Protein (RBD, mFc Tag)	40592-V05H	Antigens
S-protein	SARS-CoV-2 (2019-nCoV) Spike Protein (S1 + S2 ECD, His tag)	40589-V08B1	Antigens
S-protein	SARS-CoV-2 (2019-nCoV) Spike Protein (S1 Subunit, His Tag)	40591-V08H	Antigens
S-protein	SARS-CoV-2 (2019-nCoV) Spike Protein (S2 ECD, His tag)	40590-V08B	Antigens
N-protein	SARS-CoV-2 (2019-nCoV) Nucleoprotein/NP Antibody, Rabbit MAb	40143-R019	Antibodies
S-protein	SARS-CoV-2 (2019-nCoV) Spike Antibody, Rabbit Mab	40150-R007	Antibodies
S-protein	SARS-CoV Spike Antibody	40150-D003	Antibodies



Figure 2. Schematic presentation of the SARS-CoV-2 RNA genome (~30 kb) known to date. It encodes replicase ORF 1ab, structural proteins (S, E, M, and N), and several accessory proteins (3a, 6, 7a, 7b, and 8). It has been suggested the existence of accessory proteins 9 and 10 [46].

Table 2. Summary of nucleotide sequences for N, S, E, M, ORF1ab, ORF3, ORF6, ORF7, and ORF8 Figure 2. gene were coloured in red. Source: NCBI, Wuhan seafood market pneumonia virus isolate Wuhan-Hu-1, complete genome <https://www.ncbi.nlm.nih.gov/nucleotide/MN908947> (Accessed: 20 April 2021).

Sequence Name	Nucleic Acid Sequence
N-protein	<p>AUGUCUGAUAAUGGACCCCAAAAUCAGCGAAAUGCACCCCGCAUUACGUUUGGUGGACCCUCAGAUUC AACUGGCAGUAACCAGAAUGGAGAACGCAGUGGGGCGCGAUCAAAACAACGUCGGCCCAAGGUUAC CCAAUAAUACUGCGUCUUGGUUCACCGCUCUCACUCAACAUGGCAAGGAAGACCUUAAAUUCCUCGA GGACAAGGCGUUCCAAUUAACACCAAUAGCAGUCCAGAUGACCAAAUUGGCUACUACCGAAGAGCUA CCAGACGAAUUCGUGGGUGGUGACGGUAAAUGAAAGAUCUCAGUCCAAGAUGGUAAUUUCUACUACCU AGGAACUGGGCCAGAAGCUGGACUUCUUUUGGUGCUAACAAAAGACGGCAUCAUAUGGGUUGCAACUG AGGGAGCCUUGAAUACACCAAAAGAUCACAUUGGCACCCGCAAUCCUGCUAACAAUGCUGCAAUCGUG CUACAACUUCUCAAAGGAACAACAUUGCCAAAAGGCUUCUACGCAAGAGGAGCAGAGGGCGGCAGUCA AGCCUCUUCUGUCCUCAUCACGUAGUCGCAACAGUUCAGAAUUAACUCCAGGCAGCAGUAGGGG AACUUCUCCUGCUAGAAUGGCUGGCAAUGGCGGUGAUGCUGCUUUGCUUUGCUGCUGCUUGACAGAUU GAACCAGCUUGAGAGCAAAAUGUCUGGUAAAGGCCAACAAACAAGGCCAAACUGUCACUAAGAAAU CUGCUGCUGAGGCUUCUAAAGAAGCCUCGGCAAAAACGUACUGCCACUAAAGCAUACAAUGUAAACAA GCUUUCGGCAGACGUGGUCAGAACAAACCCAAGGAAAUUUUGGGGACCAGGAACUAAUCAGACAAGG AACUGAUUACAAACAUUGCCGCAAAUUGCACAAUUUGCCCCAGCGUUCAGCGUUCUUCGGAAUGUC GCGCAUUGGCAUGGAAGUCACACCUUCGGGAACGUGGUUGACCUACACAGGUGCCAUCAAAUUGGAUGA CAAAGAUCCAAUUUCAAGAUAAGUCAUUUUGCUGAAUAAGCAUAUUGACGCAUACAAAACAUU CCCACCAACAGAGCCUAAAAGGACAAAAGAAGGCUGAUGAAACUCAAGCCUUAACGCAGAGA CAGAAGAAACAGCAAACUGUGACUCUUCUUCUGCUGCAGAUUUGGAUGAUUUCUCCAAACAAUUGCA ACAAUCCAUGAGCAGUGCUGACUCAACUCAGGCCUAA</p>
S-protein	<p>AUGUUUGUUUUUCUUGUUUUUAUUGCCACUAGUCUCUAGUCAGUGUGUAAUCUUAACAACCAGAACUC AAUUACCCCCUGCAUACACUAAUUCUUUCACACGUGGUGUUUAUUACCCUGACAAAGUUUUCAGAUCC UCAGUUUUACAUCUACACUAGGACUUGUUCUACCUUUCUUUCCAAUGUUACUUGGUUCCAUGCUAU ACAUGUCUCUGGGACCAUUGGUACUAAGAGGUUUUGAUAAACCCUGUCCUACCAUUUAAUGAUGGUGUU AUUUUGCUUCACUGAGAAGUCUAACAUAUAAGAGGCUGGAUUUUUGGUACUAAUUAAGAUUCGAA GACCCAGUCCUACUUAUUGUUAAUAACGCUACUAAUUGUUGUUAAUAAAGUCUGUGAAUUUCAAUU UGUAAUGAUCCAUUUUUGGGUGUUUAUUACCACAAAACAACAAGUUGGAUGGAAAGUGAGUUC AGAGUUUAUUCUAGUGCGAAUAAUUGCACUUUUGAAUAUGUCUCUCAGCCUUUCUUAUGGACCUUG AAGGAAAACAGGGUAAUUUCAAAAUCUUAAGGGAUUUGUGUUUAAGAAUAUUGAUGGUUAUUUUUA AAAUAUAUUCUAAGCACACGCCUAAUUAUUUAGUGCGUGAUCUCCUCAGGGUUUUUCGGCUUUAAGA ACCAUUGGUAGAUUUUGCCAAUAGGUAAUACAUCACUAGGUUUCAAACUUUACUUGCUUUACAUAAG AAGUUAAUUGACUCCUGGUGAUUCUUCUUCAGGUUGGACAGCUGGUGCUGCAGCUUAAUUAUGUGGUU AUCUUAACCUAGGACUUUUCUAAUAAAUAUAUUGAAAUGGAACCAUUACAGAUUCUGUAGAC UGUGCACUUGACCCUCUCUCAGAAACAAGUGUACGUUGAAAUCUUCACUGUAGAAAAAGGAAUC UAUCAAAUCUUCUAAACUUUAGAGUCCAACCAACAGAUUCUAAUUGUUAAGAUUUCCUAAUUAUACAAA CUUGGCCCCUUUGGUGAAGUUUUAAACGCCACAGAUUUUGCAUCUGUUUUGGAACAGGAAG AGAAUCAGCAACUCUGUGUUCGUAUUUUCUUCUCCUAAUUAUUAUUCGCAUUAUUUCCAAUUUUAAG UGUUAUGGAGUGUCUCCUACUAAAUAUUAUGAUCUCUGCUUUAUUAUUGUCUUAUGCAGAUUCAUUU GUAAUUAGAGGUGAUGAAGUCAGACAAAUCGCUCCAGGGCAAACUGGAAAGAUUGCUGAUUAUAU UAUAAAUAUACCAGAUGAUUUACAGGCUGCGUUAUAGCUUGGAAUUCUAAACAUUCUUGAUUCUAA GGUUGGUGGUAUUUAUAAUUAACUGUAUAGAUUGUUUAGGAAGUCUAAUCUCAAACCUUUUGAGAGA GAUAUUUCAACUGAAAUCUUAUCAGGCCGGUAGCACACCUUGUAAUGGUGUUGAAGGUUUUAUUGU UACUUUCCUUUACAUAUCAUUGGUUCCAAACCAUAAUGGUGUUGGUUACCAACCAUACAGAGUA GUAGUACUUUCUUUGAACUUCUACAUGCACCAGCAACUGUUUGGACCUAAAAGUCUACUAAU UUGGUUAAAAACAAGUGUGCAAUUUCAACUUCAAUGGUUUAAACAGGCACAGGUGUUCUUCUGAG UCUAACAAAAGUUUCUGCCUUUCAACAUAUUUGGCAGAGACAUUGCUGACACUACUGAUGCUGUC CGUAUCCACAGACACUUGAGAUUCUUGACAUUACACCAUGUUCUUUUGGUGGUGCAGUGUUUA ACACCAGGAACAUAACUUAACAGGUUGCUGUUCUUUAUCAGGAUGUUUAUCUGCAGCAGAAUA CUGUUGCUAAUUAUGCAGAUCAACUUAUCUCCUACUUGGCGUGUUUAUUCUACAGGUUCUAAUGUUU UUCAAAACCGUGCAGGCUGUUUAUAGGGGCGUAACAUGUCAACAACUUAUAGAGUGUGACAUAC CCAUUGGUGCAGGUUAUAGCGCUAGUUAUCAGACUCAGACUAAUUCUCCUCGGCGGGCACGUAGUGU AGCUAGUCAAUCCAUAUUGCCUACACUUAUGCUCUUGGUGCAGAAAUAUCAGUUGCUUACUCUA AUAACUCUAUUGCCAUAACCCACAAAUUUAUUAUUAUAGUGUUAACCACAGAAAUCUACAGUGUC UAUGACCAAGACAUCAGUAGAUUGUACAAGUACAUAUUGGUGAUUCAAACUGAAUGCAGCAAU CUUUUGUUGCAAUAUGGCAGUUUUUGUACACAAUUAACCCGUGCUUUAACUGGAAUAGCUGUUG AACAAAGACAAAACACCCAAGAAGUUUUUGCACAAGUCAACAAAUUUACAAAACACCACCAA</p>

Table 2. Cont.

Sequence Name	Nucleic Acid Sequence
	UUAAAGAUUUUGGUGGUUUUAAUUUUUCACAAAUAUUACCAGAUCUCAAAAACCAAGCAAGA GGUCAUUUUAUUGAAGAUUCUACUUUCAACAAAGUGACACUUGCAGAUUGCUGGCUUCAUCAACA AUAUGGUGAUUUGCCUUGGUGAUUUGCUGCUAGAGACCUCUUUUGGCACAAAAGUUUAACGGCC UUACUGUUUUGCCACCUUUGCUCACAGAUGAAAUGAUUGCUCAAUACACUUCUGCACUGUUAGC GGUACAACUACUUCUGGUUGGACCUUUGGUGCAGGUGCUGCAUACAAAUACCAUUUGCUAUGC AAAUGGCUUUAUAGGUUUAAUGGUUAUUGGAGUUAACACAGAAUGUUCUCUAUGAGAACCAAAAAU UGAUUGCCAACCAAUUUAAUAGUGCUAUUGGCAAAAUAAGACUCACUUUCCACAGCAA GUGCACUUGGAAAACUUAAGAUGUGUCAACCAAAAUGCACAAGCUUUAAACACGCUUGUUA AACAAUCUAGCUCCAAUUUUGGUGCAAUUUCAAGUGUUUAAAUGAUUACCUUUCACGUCUUG ACAAAGUUGAGGCUGAAGUGCAAAUUGAUAGGUUGAUCACAGGCAGACUUCAAAGUUUGCAGA CAUUGUGACUCAACAAUUAUUAAGAGCUGCAGAAAUCAGAGCUUCUGCUAAUCUUGCUGCUA CUAAAUGUCAGAGUGUGUACUUGGACAAUCAAAGAGUUGAUUUUUGUGGAAAGGGCUAUC AUCUUAUGUCCUCCUCAGUCAGCACCUCUUGGUGUAGUCUUCUUGCAUGUGACUUAUGUCCCU GCACAAGAAAAGAACUUCACAACUGCUCUCCUCCAUUUUGUCAUGAUGGAAAAGCACACUUUCCUC GUGAAGGUGUCUUUGUUUCAAAUGGCACACACUGGUUUGAACACAAAGGAAUUUUUAUGAACC ACAAUCAUACUACAGACAACACAUUUGUGUCUGGUAACUGUGAUGUUGUAAUAGGAAUUGU CAACAACACAGUUUAUGAUCCUUGCAACCUGAAUUAGACUCAUUAAGGAGGAGUUAGAUAA AUUUUUUAGAUAUCAUACUACAGUUGAUGUUGAUAUAGGUGACUUCUGGCAUUUAAUGCUUC AGUUGUAAACAUUCAAAAAGAAAUUGACCGCCUCAUAGAGGUUGCCAAGAAUUUAAAUGAAU CUCUCAUCGAUCUCCAAGAACUUGGAAAGUAUGAGCAGUAUAUAAAUGGCCAUGGUACAUUU GGCUAGGUUUUAUAGCUGGCUUGAUUGCCAUAGUAAUGGUGACAAUUAUGCUUUGCUGUAUGAC CAGUUGCUGUAGUUGUCUCAAGGGCUGUUGUUCUUGUGGAUCCUGCUGCAAAUUGAUGAAGACG ACUCUGAGCCAGUGCUCAAAGGAGUCAAAUUAUUAUACACAUAA
E-protein	AUGUACUCAUUCGUUUCGGAAGAGACAGGUACGUUAAUAGUUAUAGCGUACUUCUUUUUCUUG CUUUCGUGGUAUUCUUGCUAGUUAACUAGCCAUCUUCUUCUGCGCUUCGAUUGUGUGCGUACUGC UGCAAUUUGUUAACGUGAGUCUUGUAAAACCUUCUUUUACGUUUACUCUCGUGUAAAAAU CUGAAUUCUUCUAGAGUUCUGAUCUUCUGGUCUAA
M-protein	AUGGCAGAUUCCAACGGUACUUAUACCGUUGAAGAGCUUAAAAGCUCUUGAACA AUGGAA CCUAGUAAUAGGUUUCUUAUUCUUAACAUGGAUUUGUCUUCUACA AUUUGCCU AUGCCAACAGG AAUAGGUUUUUGUAUAUAAUUAAGUUAUUUUCCUCUGGCUGUUAUGGCCAGUAACUUUAGCU UGUUUUGUGCUUGCUGCUGUUUACAGAAUAAAUGGAUCACCGGUGGAAUUGCUAUCGCAAUGG CUUGUCUUGUAGGCUUGAUGUGGCUCAGCUACUUCAUUGCUUCUUCAGACUGUUUGCGCGUACG CGUUCU AUGUGGUC AUUCAUCCAGAAACUAACA UUCUUCUCAACGUGCCACUCCAUGGCACUA UUCUGACCAGACCGCUUCUAGAAAGUGAACUCGUAUUCGGAGCUGUGAUCCUUCGUGGACAUUCU UCGUAUUGCUGGACACCAUCUAGGACGCUGUGACAUCAAGGACCUGCCUAAAAGAAUUCACUGU UGCUACAUCACGAACGCUUUCUUAUUAACAAAUUGGGAGCUUCGCAGCGUGUAGCAGGUGACUC AGGUUUUGCUGCAUACAGUCGCUACAGGAUUGGCAACUAUAAAUA AACACAGACCAUUCUCCA GUAGCAGUGACA AUUUGCUUUGCUUGUACAGUAA
ORF1ab	CCCTGTGGGTTTTACACTTAAAAACACAGTCTGTACCGTCTGCGGTATGTGGAAAGGTTATGGCTGT AGTTGTGATCAACTCCGCGAACCCATGCTTCAGTCAGCTGATGCACAATCGT
ORF3	AUGGAUUUGUUUAUGAGAAUCUUCACAAUUGGAACUGUAACUUGAAGCAAGGUGAAAUCAAGG AUGCUACUCCUUCAGAUUUUGUUCGCGCUACUGCAACGAUACCGAUACAAGCCUCACUCCCUUC GGAUGGCUUUAUUGUUGGCGUUGCACUUCUUGCUGUUUUUCAGAGCGCUUCCAAAUAUCAUACCCUC AAAAAGAGAUGGCAACUAGCACUCUCCAAGGGUGUUCACUUUGUUUGCAACUUGCUGUUGUUGU UGUAAACAGUUUACUCACACCUUUUUGCUCGUUGCUGCUGGCCUUGAAGCCCCUUUCUCUAUCUUUA UGCUUUAGUCUACUUCUUGCAGAGUAUAAACUUGUAAGAUAUAAUUGAGGCUUUGGCUUUGCU GGAAUUGCCGUUCCAAAACCAUAUUAUGAUGCCAACUAAUUUCUUGCUGGCAUACAUAU UGUUACGACUAUUGUAUACCUAAUAGUGUAACUUCUUCAAUUGUCAUUAACUUCAGGUGAUGG CACAACAAGUCCUAAUUCUGAACAUGACUACCAGAUUGGUGGUUAUACUGAAAAAUGGGAAUCU GGAGUAAAAGACUGUGUUGUAUUAACACAGUUAUCUUCACUUCAGACUAUUACCAGCUGUACUCAAC UCAAUUGAGUACAGACACUGGUGUUGAACAUGUUAACUUCUUCUUCACUUAACAAUAAAUUGUUGAU GAGCCUGAAGAACAUGUCCAAAUUCACACAAUCGACGGUUAUCCGGAGUUGUUAUCCAGUAAU GGAACCAAUUUAUGAUGAACCGACGACGACUACUAGCGUGCCUUUGUAA

Table 2. Cont.

Sequence Name	Nucleic Acid Sequence
ORF6	UUAUAUCAUCUCCAUUGGUUGCUCUUAUCUAAUUGAGAAUAUUUAUUCUCAGUUAGUGACUAG AUAUUUUUUAAUUAUGAGGUUUUAUGAUGUAAUCAAGAUUCCAAAUGGAAACUUUAAAAGUCCU CAUAAUAAUUAUGAAUAUCUCUGCUAUAGUAACCUGAAAGUCAACGAGAUGAAACAU
ORF7	AUGAAAUAUUCUUUUCUUGGCACUGAUAACACUCGCUACUUGUGAGCUUUAUCACUACCAAGAG UGUGUUAGAGGUACAACAGUACUUUUAAAAGAACCUUGCUCUUCUGGAACAUACGAGGGCAAUUA CCAUUUCAUCCUCUAGCUGAUAACAAUUUGCACUGACUUGCUUUAGCACUCAUUUUGCUUUUGCU UGUCCUGACGGCGUAAAACACGUCUAUCAGUUACGUGCCAGAUCAGUUUCACCUAAACUGUUCAUC AGACAAGAGGAAGUUAAGAACUUUACUCUCCAUUUUUCUUUAUUGUUGCGGCAAUAGUGUUUAU AACACUUUGCUUCACACUAAAAGAAAGACAGAAUGA
ORF8	AUGAAUUUCUUGUUUUCUUAGGAAUCAUCACAACUGUAGCUGCAUUUCACCAAGAAUGUAGUUUA CAGUCAUGUACUCAACAUCAACCAUAUGUAGUUGAUGACCCGUGUCCUAUUCACUUCUAUUCUAAA UGGUAUAUUAGAGUAGGAGCUAGAAAUCAGCACCUUUAAUUGAAUUGUGCGUGGAUGAGGCUGGU UCUAAAUCACCAUUCAGUACAUCGAUAUCGGUAAUUUAACAGUUUCCUGUUUACCUUUUACAAU UAAUUGCCAGGAACCUAAAUUGGGUAGUCUUGUAGUGCGUUGUUCGUUCUAUGAAGACUUUUAGA GUAUCAUGACGUUCGUGUUGUUUAGAUUUCAUCUAA

The as-mentioned PCR handling procedures require high equipped laboratory and skilled labour that lower detecting efficiency and capacity per each run. Thus, several other PCR derivative methods, including reverse transcription loop-mediated isothermal amplification (RT-LAMP) and clustered regularly interspaced short palindromic repeats (CRISPR)-based assay, are currently flourishing. It has been shown that RT-LAMP can amplify nucleic acid under isothermal conditions in the range of 65 °C that does not require high-cost equipment, and RT-LAMP assay showed a lower LOD (~ 80 copies mL^{-1}) than general RT-PCR (~ 100 copies mL^{-1}) [49–52]. In contrast, it is less sensitive than PCR to inhibitor in the case of complex samples, including blood and serum, as RT-LAMP utilizes Bst DNA polymerase rather than Taq polymerase. CRISPR-based assay (e.g., Cas 12) has been introduced as a novel and highly sensitive tool with low-resource settings requirement for detecting the SARS-CoV-2 [53]. The claimed LOD of CRISPR-Cas12-based assay for probing the virus was 10 copies/ μL . Nevertheless, the CRISPR-based kits are still in the developmental stage that needs further clinical validation.

1.3.6. Recently Advanced Biosensors as Alternative Viral Detection Methods

Numerous advanced biosensors have been recently developed for the early recognition of viral diseases in humans. The sensors should be minimally invasive, fast performing, highly sensitive, low-cost, user-friendly, and highly accessible for their raw materials. Recently developed nanomaterials provide distinctive characteristics, such as small size, large surface area, and unique physical/optical properties for versatile applications, including biomarkers detection. Amongst the nanomaterials harnessed as biosensors, two-dimensional (2D) nanocomposites are promising platforms as nanosensors for probing viruses due to their high surface area, good biocompatibility, and simple structure, and, more importantly, the unique electronic/optoelectronic/electrochemical properties for easy functionalization [54]. Hence, these excellent properties render them a prominent position in the next-generation nanotechnologies for viral recognition. To the best of our knowledge, limited literature reviews provide comprehensive discussions of applying 2D transition metal dichalcogenide (TMD) nanocomposites for viral sensing and detection, especially before and during the COVID-19 pandemic. As this pandemic is still ongoing and the fluctuation of the infection cases is not stable, the social distance and the work-from-home regulation policy of different workplaces are of great restrictions to researchers for continuing the research, such as developing TMD-related biosensors [55]. In this review, we present an overview of recent biosensors that utilize emerging 2D TMD-based materials and their derivatives responsible for screening lethal viruses before the outbreak (before December

2019) and during the outbreak. We introduce the structures, physiochemical properties, functionalization, and biosensors designs of the 2D TMD nanocomposites. Finally, we discuss the advantages and limitations of those nanocomposites for virus detection.

2. Two-Dimensional Nanocomposites

Carbon-based nanomaterials such as graphene and its derivatives have been extensively developed and investigated due to their exceptional physical and chemical properties. Several excellent recent reviews and articles have highlighted the critical roles and the demonstrations of utilizing graphene-based materials in detecting human viruses before and during the pandemic [56,57]. On the other hand, the application of alternative 2D layered nanocomposites such as transition metal dichalcogenides (TMD, e.g., MoS₂, WS₂, and MoSe₂) and metal oxides (MO_x—e.g., MoO₃ and WO₃) are low cost with attractive physical and chemical properties as novel optical/electronic/chemical biosensors (Figure 3). These superior properties permit them on various sensing mechanisms, including optical sensation through chemiluminescence, surface plasmon resonance (SPR), and electrochemistry for a field-effect transistor (FET, voltage-current under gating control) by p-n junctions for detecting specific biomolecules and gases [54,58,59]. For instance, 2D Mn oxides-based materials exhibit a powerful catalytic property that has been employed as nanoenzymes for catalyzing the hydrolysis of biomolecules via peroxidase-like activity, thereby producing electrochemical/electrochemiluminescence signals as the detection readouts [60–62]. While metal oxides may play a more critical role in chemical catalysis and fuel cells, TMDs can be a significant part of sensor developments [63,64]. However, very limited reviews have discussed the potential application of TMD-based biosensors for probing proteins and nucleic acids of viruses. In the following sections, we explore and discuss the properties and functionalization of TMDs that are useful for engineering highly sensitive and effective viral sensors.

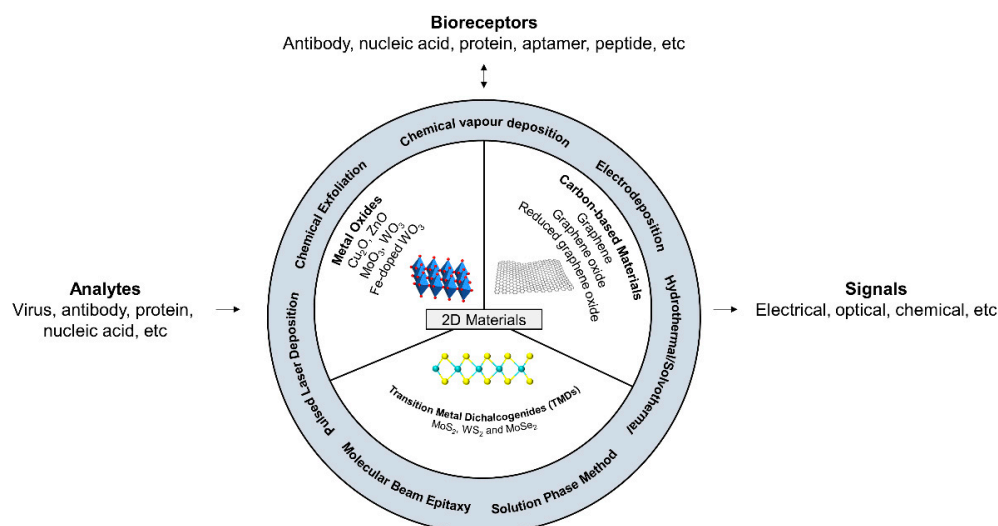


Figure 3. Schematic illustration of general strategies for fabricating 2D materials, mainly transitions metal dichalcogenides (TMDs), carbon-based materials, and metal oxides as biosensors engaged with bio-receptors to detect various analytes and generate signals corresponding to the concentration of analytes.

2.1. Transition Metal Dichalcogenides (TMDs) on Biosensing

2.1.1. Types of Elements as the Critical Parameters for Biocompatible Sensors

TMDs monolayers are atomically thin (~ 6 to 7 \AA) semiconductors consisting of type MX_2 , where M is a transition metal atom from IVB–VIB (Ti, Zr, Hf, V, Nb, Ta, Mo, Tc, W, Re, Co, Ni, Rh, Ir, Pt or Pd) and X is a chalcogen atom (S, Se or Te). Hence, they are considered analogs of graphene with a layered structure [65]. Importantly, the bandgap is a critical characteristic of TMDs that influences transistor on/off ratio and chemical stability and

durability in ambient conditions. Graphene is a zero-bandgap semiconductor, leading to a low on/off ratio limit in FET. Generally, TMD elements with smaller atomic numbers show larger bandgap, and chalcogen elements greatly influence this bandgap (e.g., WSe₂: 1.6 eV, MoSe₂: 1.6 eV, MoS₂: 1.8 eV, and WS₂: 2.1 eV). The overall structure and methodology of TMDs preparation have been summarized in detail in previous reviews [58,66].

Cytotoxicity of TMDs is a great concern for biosensing in vitro and in vivo on a large scale when considering extensive labour work for screening SARS-CoV-2 infection cases. Specifically, Teo et al. showed the graphene with the highest toxicity on human lung carcinoma epithelial cells (A549), followed by WSe₂, MoS₂, and WS₂ [67]. They concluded that MoS₂ and WS₂ induced very low cytotoxicity to the cells compared to the other 2D materials and the biocompatibility of S was better than that of Se in terms of chalcogen. Besides, it has been suggested Te showing latent toxicity (e.g., neurotoxicity and cytoskeleton disruption) to humans [68]. Therefore, S is the best candidate as the chalcogen combination with M.

In terms of photoluminescence-based biosensors, TMDs are also excellent fluorescence quenchers via electron/charge transfer (ET) to “turn off” fluorophores at the initial state without the target [69]. For instance, TMDs provide a high 2D surface area for single-strand DNA (ssDNA) to adsorb on their surface via van der Waals force theoretically, thereby efficiently quenching the adsorbed fluorophores-bearing ssDNA. This mechanism permits the “turn on” of the fluorescence when ssDNA hybridizes with the target nucleic acid sequence, forming double-stranded DNA that has a weak interaction with the TMDs and detaches from the TMDs platforms. Although MoS₂ and WS₂ showed a similar extent of quenching efficiency (Q_e) towards FAM-labeled probes (71% and 75%, respectively), MoS₂ exhibited a stronger affinity for the nucleic acids than that of WS₂ [70]. This affinity determines detection capacity (reservoir of probing reagent). In short, the choice of elements in TMDs decides the performance of TMD-based biosensors.

2.1.2. Polymorph Types and Morphologies of TMDs Alter Sensor Performance

Polymorphs are phases that influence the bonding and configurations in TMDs crystals. Typically, there are three polymorphs of TMDs: single-layered trigonal (1T), double-layered hexagonal (2H), and triple-layered rhombohedral (3R). Nevertheless, TMD often forms 1T (metallic/semi-metallic) and 2H (semi-conductive with visible-range bandgap) when exfoliated into a single layer [71]. Both phases of TMF possess their own characteristics. For example, Lan et al. demonstrated phase-dependent fluorescence quenching efficiency (Q_e) of MoS₂ nanosheets that 1T phase MoS₂ exhibited much higher fluorescence Q_e (98%) than those in 2H phase MoS₂ (2%) at a similar concentration (4.65 g mL⁻¹) through the enhanced metallic conductivity for the improved ET-mediated fluorescent quenching [72]. Therefore, 1T phase MoS₂ is suitable for designing biosensing based on fluorescence quenching [73]. In contrast, the bandgap of 2H phase MoS₂ is adjustable. When the number of layers in MoS₂ crystal increases from monolayer to bulk, the lowest conduction band near the Γ point shifts to lower energy [74]. This increased number of layers in MoS₂ crystals change them from indirect to direct semiconductors (Figure 4). Therefore, the properties of 2H phase TMDs are suitable for designing electronic devices, such as FET and solution-gated transistor (SGT) biosensors [75]. 1T phase and 2H phase TMDs nearly have opposite physiochemical properties. Recent emerging TMDs-based approach biosensors have been achieving a dynamic and reversible “phase transition” (e.g., the transition between monoclinic (1T) and 2H) by external stimuli such as the electrostatic-doping method [76] and strain-induction [77]. Thus far, this transition implies the possible coexisting of different types of biosensors (e.g., FET, SGT, fluorescence, etc.) for probing different types of biomarkers such as protein and nucleic acids.

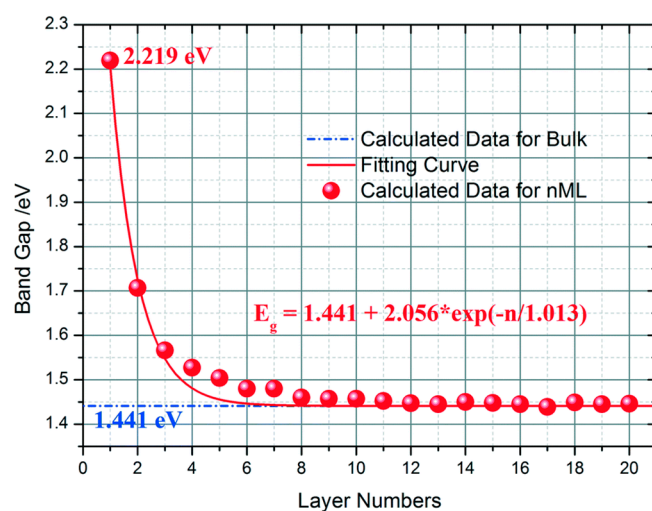


Figure 4. The bandgap of 2H-MoS₂ nanosheets with respect to the layer number; the dot-dashed line represents the corresponding value for the bulk. The figure is reprinted with permission from Ref. [74]. Copyright Royal Society of Chemistry. (2019).

Laterally or vertically aligned geometries TMDs exhibit different physicochemical properties from conventional TMDs. Based on the size, shape, and geometries of TMDs, they can be classified into the followings: (1) nanodots (NDs), (2) nanosheets (NSs, lateral size < 100 nm), (3) nanoflakes/films (NFs, lateral size > 100 nm), (4) nanorods (NRs) and (5) nanofibers (NFs). These different geometries can create heterojunctions, which may overcome the low optical cross-section of MoS₂ for enhanced absorption and improved photo-detectivity [78,79]. For instance, small sizes of NSs and NDs provide high active surface area and depletion layer at the material interfaces, and hence they are suitable for electrochemical, fluorescent, chemiluminescent, and colorimetric biosensors.

2.1.3. TMDs-Based Disease-Related Proteins Biosensors

Direct detection of virus (~100 nm) and bacteria (several micrometers) may require less sensitive platforms due to the large physical size. It has been demonstrated the usage of silicon nanowire to detect a single virus and graphene to detect a single bacterium, based on the FET mechanism [80,81]. Nevertheless, the operation of viral/bacterial-containing samples may be dangerous to general labours and not appropriate at a low biosafety level area. On the other hand, the handling of their extracted components from the samples, such as structural proteins, which have a much smaller size (<10 nm) and require biosensors with higher sensitivity than detecting whole viruses/bacteria. Micro/nanodevice-based FET platforms are generally a promising tool for detecting single molecules through the gating effect to achieve high sensitivity. The creation of bandgap in carbon nanotubes or graphene needs complex processing and is usually low yield that hampers the application of carbon materials-based FET [82]. In contrast, TMDs-based FET (e.g., MoS₂) is highly advantageous for scaling the FET biosensor device with a low-power operation because of the as-mentioned properties. A summary of TMD-based biosensors via various mechanisms to detect disease-related proteins has been enlisted in Table 3.

Table 3. Recent 2D TMD-based materials and related mechanisms for probing disease-related proteins and their sensing performances.

Materials	Mechanism	Analytes	Detection Limit Range	LOD	Response Time	Ref. & Year
Flexible MoS ₂ sheets	FET	Ebola VP40	fM–pM level	fM level	15 min	[83] 2019
DNA-MoS ₂ nanosheets	Fluorescence	Thrombin	0.5–100 nM	300 pM	10 min	[84] 2014
Flexible MoS ₂ sheets	FET	Prostate cancer antigens	1 pg mL ⁻¹ –1 µg mL ⁻¹	1 pg mL ⁻¹	~real-time	[85] 2017
Few-layered MoS ₂ sheets	FET	Prostate cancer antigens	10–5–75 ng mL ⁻¹	10–5 ng mL ⁻¹	20–30 min	[86] 2016
Multilayer MoS ₂	FET	MMP-9	1 pM–10 nM	1 pM	2 h (incubation time)	[87] 2019
Graphene quantum dots/MoS ₂ nanosheets	Fluorescence	Epithelial cell adhesion molecules	3–54 nM	450 pM	2 h (incubation time)	[88] 2017
Au/MoS ₂ /Au multilayer	Electrochemical	HIV gp120	0.1 pg mL ⁻¹ –10 ng mL ⁻¹	0.066 pg mL ⁻¹	N/A	[89] 2019
MoS ₂ @Cu ₂ O-Pt	Electrochemical	Hepatitis B surface antigen	0.5 pg mL ⁻¹ –200 ng mL ⁻¹	0.15 pg mL ⁻¹	1 h (incubation time)	[90] 2018
Au@Pd/MoS ₂ @multiwalled carbon nanotubes	Electrochemical	Hepatitis B e antigen	0.1 pg mL ⁻¹ –500 pg mL ⁻¹	26 fg mL ⁻¹	1.5 h (total incubation time)	[91] 2018
MoS ₂ -rGO	Electrochemical	Vi polysaccharide antigen	0.1–1000 ng mL ⁻¹	100 pg mL ⁻¹	30 min (incubation time)	[92] 2018
MoS ₂ -AuNP/ITO	Electrochemical	Dengue NS1 antigen	0.04–2 µg mL ⁻¹ in primary infection; 0.01–2 µg mL ⁻¹ in secondary infection	1.67 ng mL ⁻¹ for standard; 1.19 ng mL ⁻¹ for spiked samples	~25 min	[93] 2018
MoS ₂ sheets	FET	Kinase Cdk5/p25	pM–µM level	38 pM	~5 min	[94] 2019
Ag/MoS ₂ /rGO	Electrochemical	Carcinoembryonic antigen	0.001–80 ng mL ⁻¹	0.3 pg mL ⁻¹	1 h (incubation time)	[95] 2020
Tellurene/MoS ₂ Nanosheets	Optical/SPR	S protein or SARS-CoV-2 specimen	0–301.67 nM for S protein; 0–67.8762 nM for SARS-CoV-2 specimen	Phase sensitivity: 8.4069 × 10 ⁴ degree/RIU (n _{bio} = 0.0012)	N/A	[96] 2020
Aptamer-cellulose acetate-MoS ₂	Electrochemical	Troponin I	10 fM–1 nM	10 fM	N/A	[97] 2021

For instance, Yoo et al. fabricated a highly sensitive MoS₂ sheets-based flexible biochip to detect prostate-specific antigen (PSA), which is a widely adopted biomarker of prostate cancer [85]. The MoS₂ FET biosensor allowed a high affinity for the physisorption of PSA

antibodies and hence measured the variation of on/off-current levels upon the binding of PSA with anti-PSA antibodies. This device exhibited high-performance electrical properties and mechanical durability under different mechanical stress with LOD at 1 pg mL^{-1} , which is several orders of magnitude more sensitive than the clinical cut-off concentration ($\sim 4 \text{ ng mL}^{-1}$). More importantly, such device exhibited real-time monitoring of the off-current level over various PSA concentrations and maintained the stabilized off-current level for 2–3 min, with or without bending stress (bending radius: 10 mm). Their findings demonstrated the use of the MoS_2 FET biosensor as a powerful tool for real-time point-of-care (POC) diagnostics of disease-related proteins.

2H phase TMDs can also be applied to an electrochemical strategy for detecting proteins. However, the preparation of large sheet size, high yield, and high-quality 2H- MoS_2 has been a great challenge as the previous synthetic methods relying on micromechanical cleavage, chemical intercalation, and ultrasound-promoted shear exfoliation limitedly yield (<40%) single-layer MoS_2 sheets [98–100]. Zhang et al. developed an array of the biosensor by restacking 2H- MoS_2 flakes into a thin film on the flexible polyimide support via cathodic exfoliation in the organic electrolyte to detect VP40 matrix protein from the Ebola virus down to picomolar levels (Figure 5a) [83]. They showed that the synthetic process avoided surface oxidation to preserve MoS_2 sheets with an intact crystalline structure and structure integrity with high yield ($\sim 70\%$) and large size ($\sim 50 \text{ }\mu\text{m}$) (Figure 5b). By incorporating receptors (VP40 antibodies) onto this platform, the device was able to change current after VP40 proteins binding with the immobilized antibodies from 5.72 pM to 57.2 nM . Also, the antibody-antigen complex could be dissociated by incubating with glycine-based regenerated buffer to VP40 detection repeatedly (Figure 5c–f). These findings outline the excellent performance of the MoS_2 sheets-based biosensor for precise and rapid detection of the presence of viral proteins, particularly useful for probing SARS-CoV-2 proteins in the current pandemic.

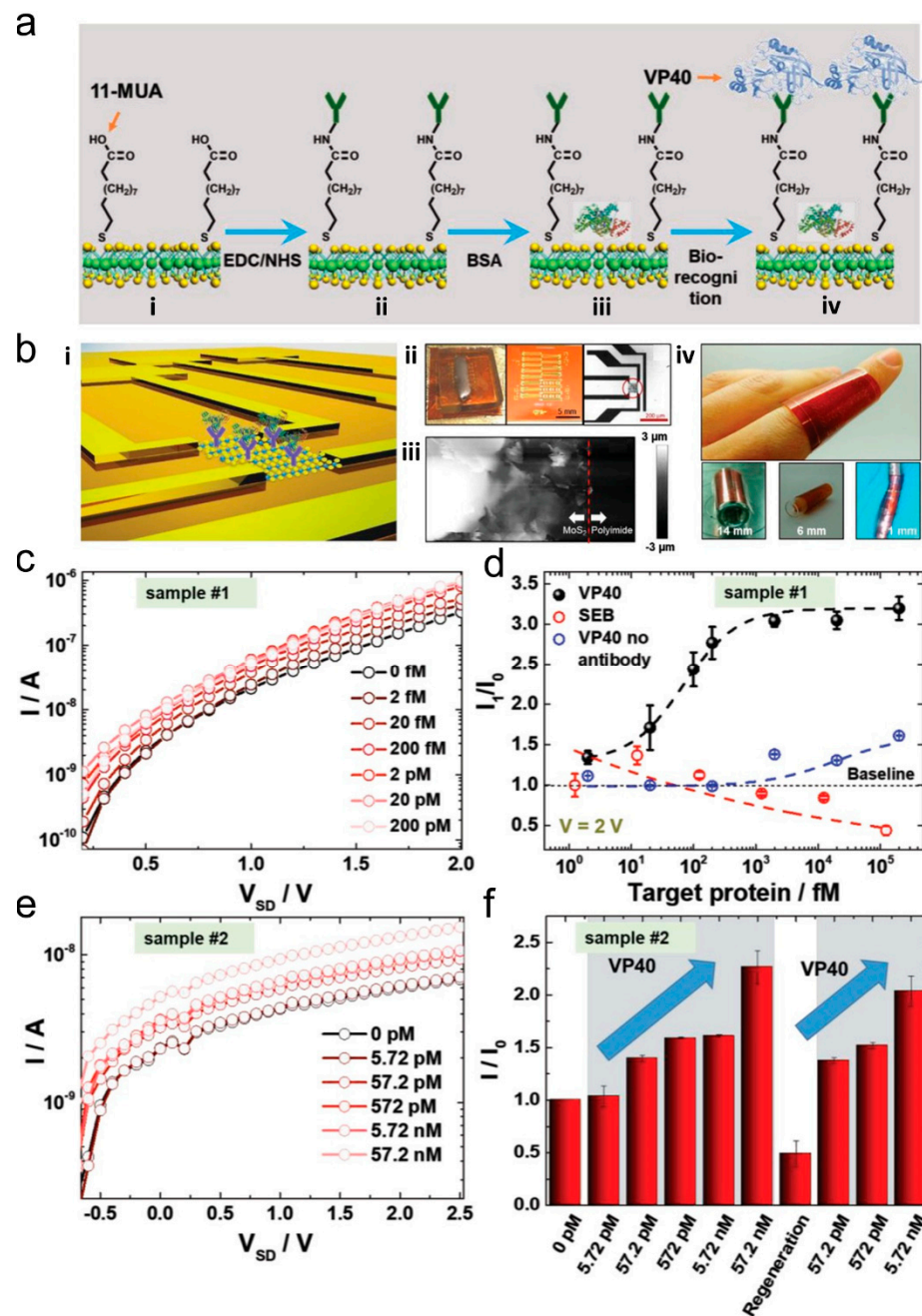


Figure 5. Electrochemically exfoliated MoS₂ for stacking MoS₂ flakes on the polyimide substrate to detect Ebola virus VP40 matrix protein. (a) Biofunctionalization of the MoS₂ nanoflakes for capturing VP40. (b) Fabrication of flexible MoS₂ biochip with VP40 sensors. (c) Electric current measurements after the incubation of various VP40 concentrations on a sensor with a high amount of flakes. (d) Calibration of the response and comparison with control sensors (no antibody and non-specific antigen). (e) Repeated electric current measurements after the incubation of various VP40 concentrations on a sensor with a low amount of flakes. (f) The device could be reused to probe VP40 after antibody-antigen dissociation, and repetition of the tendency result remained similar after analyte incubation. Figures are re-arranged and reprinted with permission from Ref. [83]. Copyright Wiley-VCH. (2019).

DNA aptamers that recognize a protein can be generated by systematic evolution of ligands by exponential enrichment (SELEX) from random-sequence nucleic acid pools [101]. By the usage of aptamers, the probing component of the biosensor can be simplified with less bulkiness. Recent work showed the application of graphene quantum dots

(GQDs)-labelled aptamer physically adsorbed on MoS₂ nanosheets for detecting epithelial cell adhesion molecules (EpCAM), which are glycosylated membrane proteins typically expression on the surface of circulating tumour cells (Figure 6a) [88]. The fluorescent signals of GQDs were quenched by MoS₂ nanosheets via FRET and recovered when approaching EpCAMs due to the detachment of GQDs-aptamers from MoS₂ nanosheets. More importantly, their findings showed that the platform was able to sense both individual EpCAM proteins (Figure 6b,c) and intact membrane proteins from MCF-7, a breast cancer cell line. Instead of immobilizing antibodies, TMD-based materials can be integrated with nucleic acid materials as a low-cost and effective protein sensor.

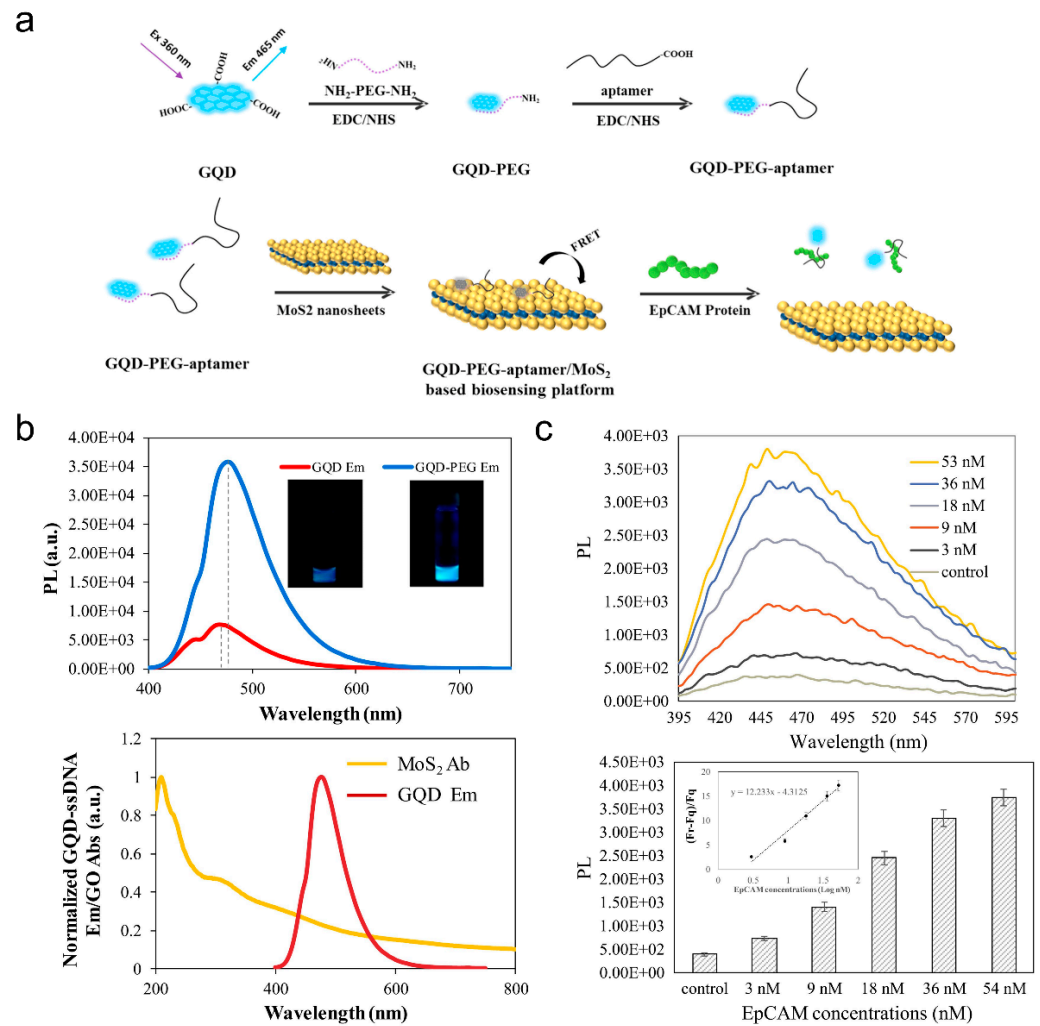


Figure 6. Harnessing aptamer-bearing graphene quantum dots (GQDs-PEG-aptamer) coupling onto MoS₂ nanosheets (GQDs-PEG-aptamer/MoS₂) as a FRET biosensor for epithelial cell adhesion molecule (EpCAM) detection. (a) Schematic illustration of the sensing mechanism of GQDs-PEG-aptamer/MoS₂ FRET nanosensor. (b) Photoluminescence (PL) intensity and emission spectra GQD with absorption spectra of MoS₂. (c) Fluorescence recovery spectra and peak fluorescence signal of the FRET biosensor against various EpCAM concentrations. Figures are re-arranged and reprinted with permission from Ref. [88]. Copyright Elsevier Ltd. (2017).

In 2020 of the COVID-19 period, Peng X. et al. demonstrated a near-infrared (NIR) plasmonic biosensor employed for specific detection of SARS-CoV-2 and its spike glycoprotein [96]. This platform was constructed by mutual Van der Waals stacking consecutive layers of rutile prism, BK7 glass, indium tin oxide (ITO) film, 2D tellurene nanosheets, and MoS₂-COOH (from the bottom to the top layers). Conventionally, metal films have significant drawbacks such as easy oxidation (Ag film), easy aggregation (Au film), or

band-to-band transitions (Au film), while ITO films can overcome these drawbacks and can support SPR in the NIR region. Moreover, ITO thin film is usually coated onto a thin BK7 glass slide for enhancing biosensing performance. Together with the excitable SPR enhancement in tellurene-MoS₂-COOH by NIR (p- or s-polarized incident light at 1550 nm), the whole heterostructures optimized SPR signal for describing the binding interactions between the -COOH and the -NH₂ from ACE2 protein or S protein of the SARS-CoV-2. This binding varied the refractive index of the platform that affects the perturbation for enhanced electromagnetic field, which can be evaluated by measuring reflectivity, redshift in SPR angle, and the change in differential phase between p-polarized and s-polarized light. The author utilized the obtained differential phase for determining the concentration of S protein or SARS-CoV-2 specimen, which showed linear relationships with the change in differential phase (from 0 nM to 301.67 nM for S protein and 0 nM to 67.8762 nM for SARS-CoV-2 specimen). This optical-SPR approach shows great promise for detecting practical biological samples, one-step rapid detection, and low labour cost, compared to traditional ELISA methods for examining SARS-CoV-2-related proteins.

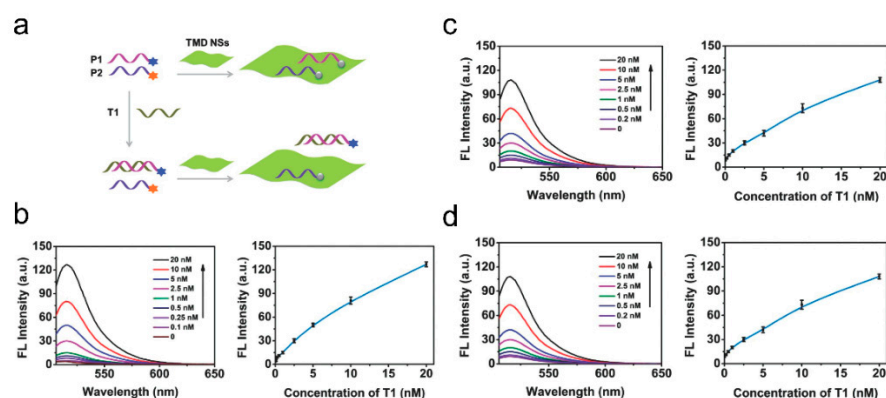
2.1.4. TMDs-Based Disease-Related Nucleic Acids Biosensors

One of the conventional methods to probe the target nucleic acid sequence (DNA or RNA) is to utilize quenched fluorescent probe-bearing ssDNA by a specific quencher, typically via electron transfer (ET) or fluorescence resonance energy transfer (FRET) [102,103]. The absorption spectrum of the quencher (Q) must overlap with the fluorescence spectrum of the reporter (R) with an effective quenching distance (10 to 100 Å range) between donor and acceptor. The close distance can be conventionally achieved by linkage of R and Q to both ends of a hairpin DNA that can hybridize with complementary strand DNA forming dsDNA and uncoil the hairpin DNA to extend the distance for diminishing the quenching efficiency to recover the desired fluorescent signal from R. Alternatively, the fluorescent probe-bearing ssDNA can be physically coupled onto 2D materials such as graphene oxide (GO) via π - π interactions (and also hydrogen bonds) between the ssDNA and graphene or MoS₂ via van der Waals' force. The 2D materials can closely quench the fluorescence by FRET [104]. Under the FRET principle, GO showed the highest DNA sensitivity compared to TMDs nanosheets (MoS₂ and WS₂) due to different DNA desorption capacities among these nanosheets. However, their LODs against a specific cDNA sequence were similar (several nano-molarity levels).

Before the emergence of COVID-19, different types of efficient TMDs-based biosensors have been designed to achieve rapid response in the presence of specific nucleic acids of virus diseases (e.g., HIV, Ebola virus) [83,105]. These 2D nanosheets-based biosensors offer a simple detection process for probing specific nucleic acids sequences without complicated platform design and equipment (Table 4). One of the well-known examples demonstrated by Zhang et al. showed the application of single-layer TMD nanosheets (MoS₂, TiS₂, and TaS₂) for rapid, sensitive, and multiplexed detection of influenza A virus DNA (subtypes: H1N1 and H5N1) [106]. The multiplexity was based on adsorbing dye-labelled ssDNA (FAM-labelled H1N1 targeting ssDNA and Texas red-labelled H5N1 targeting ssDNA) onto the nanosheets (Figure 7a). Hence, the recovery of fluorescent intensity at a particular wavelength indicated the presence and the concentration of the target sequence after incubating with a DNA-containing sample. Their work claimed that TaS₂-based detection showed the highest sensitivity against H1N1 ssDNA (LOD: 50 pM) compared to MoS₂ (LOD: 100 pM) and TiS₂ (LOD: 200 pM) due to their respective quenching abilities and affinities with the ssDNA and dsDNA (Figure 7b-d). More importantly, the platform was able to target DNA within 5 min (for each TMD nanosheets). This study illustrated the new insight into the design of TMDs-based multiplexed sensors for viral nucleic acid detection.

Table 4. Recent 2D TMD-based materials and related mechanisms for probing disease-related nucleic acids and their sensing performances.

Materials	Mechanism	Analytes	Linear Range	LOD	Ref. & Year
MoS ₂ sheets	Electrochemical	Chikungunya virus DNA	0.1 nM–100 μM	3.4 nM	[107] 2018
AuNP/MoS ₂ sheets	FET	Fetal cell-free DNA fragments	100 aM–1 fM	100 aM	[108] 2019
MoS ₂ /THT-MB	Fluorescence	miRNA	0.1 nM–100 nM	5.9 pM	[109] 2019
FAM-labelled ssDNA MoS ₂ , TiS ₂ , and TaS ₂ nanosheets	Fluorescence	Influenza A virus (H1N1 and H5N1)	0–5 nM	0.2, 0.1, and 0.05 nM, respectively	[106] 2015
PANI-MoS ₂	Electrochemical	Cauliflower mosaic virus 35S	1 fM–1 μM	2 fM	[110] 2016
PANI-MoS ₂ -Pt	Electrochemical	Calf-thymus DNA	1 fM–1 μM	1 fM	[111] 2018
MoS ₂ -thionin	Electrochemical	dsDNA	0.09 ng mL ⁻¹ –1.9 ng mL ⁻¹	0.09 ng mL ⁻¹	[112] 2014
MoS ₂ /graphene film	Electrical/optical	Oligonucleotides	1 aM–1 fM (non-linear)	1 aM	[113] 2014
MoS ₂ nanosheet-modified dendrimer droplet microarray	Fluorescence	HIV-1, HIV-2, ORF1ab, and N protein gene	N/A	50 pM	[114] 2020
ZnO (NPs) doped MoS ₂	FET	Hepatitis B virus	0.5 pM–50 μM	1 fM	[115] 2021
MoS ₂ -thionine-carbon nanodots	Electrochemical	InIA gen of <i>Listeria</i> and ORF1ab of SARS-CoV-2	100 fM to 50 nM and 1 pM to 1 nM, respectively	67.0 fM and 1.01 pM, respectively	[116] 2021

**Figure 7.** Multiplexed detection of H5N1 subtypes (T1 and T2) DNA by single-layer TMD nanosheets via FRET mechanism. (a) Schematic illustration of the sensing mechanism by multiplexed fluorescent DNA detection. Fluorescent spectra and intensity of (b) MoS₂, (c) TiS₂, and (d) TaS₂, respectively. Figures are re-arranged and reprinted with permission from Ref. [106]. Copyright Wiley-VCH. (2014).

Electrochemical biosensors are another promising approach for detecting nucleic acid. Yang et al. developed a label-free, and self-signal amplification platform for sensing cauliflower mosaic virus 35S (CaMV35S) DNA based on nanocomposites of MoS₂ and conductive polymers, polyaniline (PANI, Figure 8) [110]. By integrating PANI (organic polymer) into MoS₂ (inorganic materials), the electronic conductivity of the whole composite was much improved with a low electron transfer resistance (R_{et}). Moreover, the rich π structure PANI platform allowed strong immobilization of probing DNA sequence through π - π^* interaction that increased R_{et} . The hybridization of the target DNA with

the immobilized ssDNA did not detach the whole dsDNA but increased its R_{et} , thereby successfully sensing CaMV35S. The increase of MoS_2 dosage (optimum dosage at 0.054 g) enhanced the sensitivity and linearity of the platform by influencing the DNA absorption capacity. Ultimately, the linear range and LOD of this platform were 1 fM to 1 μ M and 2 fM, respectively. These findings demonstrated the importance of TMD-polymer nanocomposite as an electrochemical indicator of viral nucleic acid sequence.

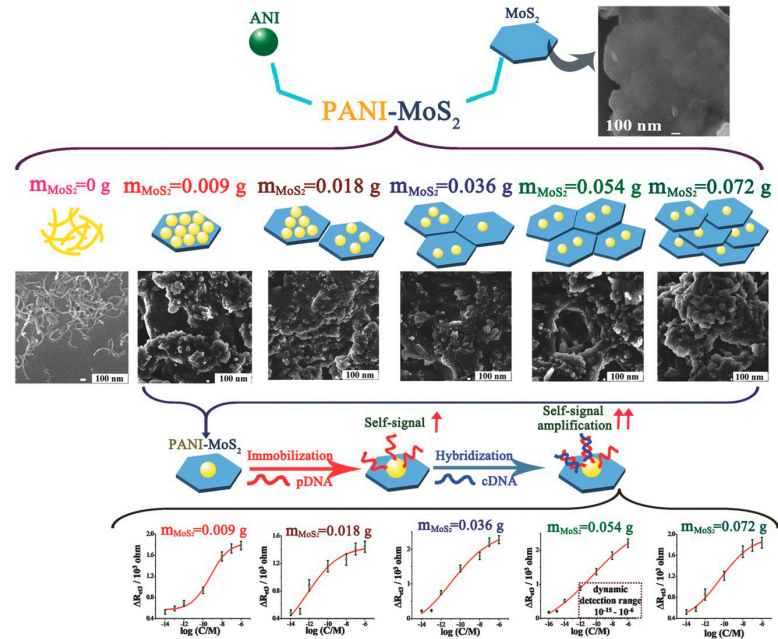


Figure 8. Schematic illustration of conductive polymer polyaniline (PANI)- MoS_2 nanocomposites through facile oxidation polymerization aniline monomer on the thin-layer MoS_2 matrix for electrochemically sensing cauliflower mosaic virus 35S DNA. The effect of DNA sensitivity of this platform is based on the dosage of MoS_2 with PANI. The figure is adopted and reprinted with permission from Ref. [110]. Copyright Wiley-VCH. (2016).

During the outbreak of the COVID-19 pandemic in 2020, our research team has reported MoS_2 nanosheet-modified dendrimer droplet microarray (DMA) for simultaneously rapid and sensitive detection of five viral genes, HIV-1, HIV-2, ORFlab, and N genes of SARS-CoV-2 and M gene of Influenza A (Figure 9) [114]. MoS_2 nanosheets were conjugated onto cysteamine-containing DMA (MoS_2 -DMA), serving as acceptors substrate, and subsequently interacted with multiple fluorescent dye-labeled oligonucleotide probes serving as donors for FRET assays. Together, the microarray could be designed as an array $N \times M$, where N is the number of fluorescence colors and M is the number of sensing sections. Our results showed that those viral target genes were able to hybridize with the fluorescently labelled oligonucleotides, thereby triggering the “turn-on” of the fluorescence signal. Importantly, our platform only required a small sample size (<150 nL) for simultaneous detection of HIV-1 and HIV-2 nucleic acids with a LOD of 50 pM within 1 h. The fluorescent signal of each microarray was captured by a digital camera at various time points. This microarray viral biosensor provides a high-throughput screening platform for simultaneous monitoring of multiplexed viral nucleic acids screening, such as the SARS-CoV-2 viruses, from a small sample size.

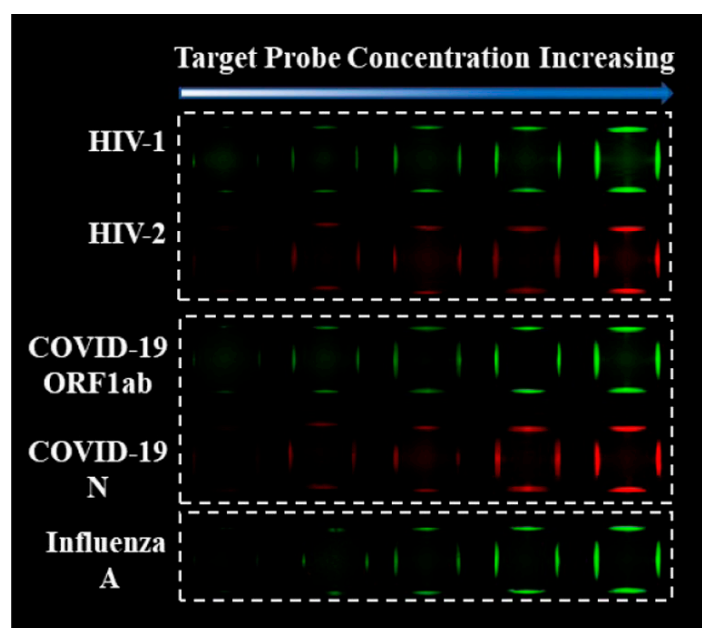


Figure 9. MoS₂-DMA FRET sensing platform for the detection of HIV-1 and HIV-2 genes; COVID-19 ORF1ab and N genes; M genes of influenza A. Figure is reprinted with permission from Ref. [114]. Copyright American Chemical Society. (2020).

In 2021, Lorenzo E. et al. developed an electrochemical biosensor applied to detect DNA sequences from the InIA gen of *Listeria monocytogenes* or the open reading frame (ORF1ab) of the SARS-CoV-2 (Figure 10) [116]. This biosensor consisted of thiolated single-stranded oligonucleotides (Probe-SH) conjugating to 2H-polytype MoS₂ sheets that were immobilized on carbon screen-printed electrode (CSPE) electrodes as the sensation platform. After the platform incubating with samples containing target nucleic acids for hybridizing with the Probe-SH, they added Thi-CNDs as the hybridization redox indicator. This accumulation of Thi-CNDs on the dsDNA layer formed on the electrode surface exhibited enhanced electrochemical signal measured by differential pulse voltammograms (DPV), and the signals linearly increased from 100 fM to 50 nM (LOD: 67.0 fM) for detecting *Listeria monocytogenes* or from 1.00 pM to 1.00 nM (LOD: 1.01 pM) for detecting SARS-CoV-2 virus nucleic acids. Notably, the authors attempted to detect real *Listeria monocytogenes* whole genomic DNA samples and found that the results correlated well with the results from a specific sequence from a gen. This latest study indicated the potential application of TMD materials to fabricate electrochemical biosensors to sense SARS-CoV-2 and is amenable to any pathogen for which the DNA has been sequenced.

2.1.5. Metal/Carbon-TMDs Nanocomposites Optimize Biosensor Performance

Transition metal oxides (TMO), such as cuprous oxide (Cu₂O) nanocrystals, have been recognized as a great molecular sensor component because of their high electrochemical and redox activity, environmentally friendly elements, and good electrocatalytic performance such as reducing H₂O₂ [117–119]. The performance of Cu₂O-based sensors, such as immunosensor against particular proteins, depends on the electrocatalytic performances to reduce H₂O₂. This catalytic activity can be assisted by integrating Cu₂O with noble metal NPs such as platinum (Pt) NPs that further enhance the electrocatalytic properties of the composites [120]. However, the photolysis stability of Cu₂O under light exposure and a humid environment has been the main issue that restricts its versatile applications, including biosensing in the long term [121]. To improve Cu₂O biosensor stability, previous studies attempted to combine Cu₂O nanocrystals with TMD materials such as MoS₂ nanoflakes for enhanced electronic transmission capability, catalytic performance, and dispersibility for sustained applications.

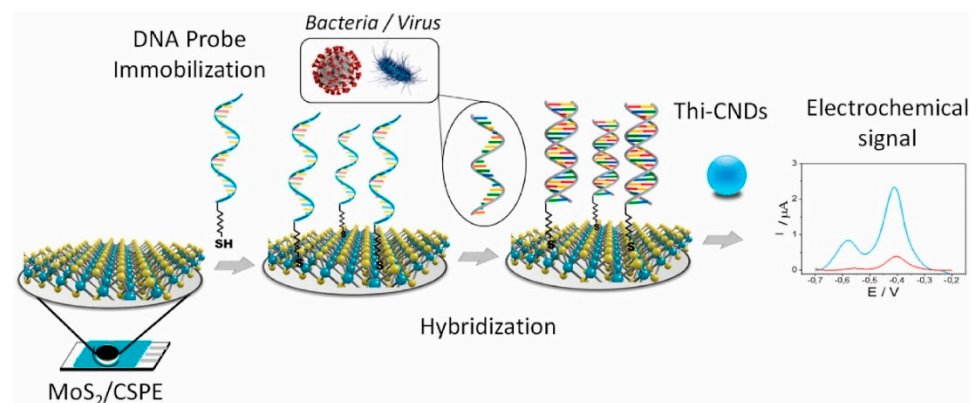


Figure 10. Schematic diagram of a DNA-MoS₂ platform and thionine-carbon nanodots for detecting the nucleic acids of ORF1ab in SARS-CoV-2 and DNA of *Listeria monocytogenes*. The figure is reprinted with permission from Ref. [116]. Copyright Elsevier Ltd. (2021).

Accordingly, Au/graphene/MoS₂ nanohybrid heterostructures are considered as a huge potential for developing various types of outstanding biosensors [122]. Gold nanoparticles (AuNPs) possess large surface areas, good colloidal stability, and biocompatibility, providing a good pathway for electron transfer and enhance the immobilized amount of useful biomolecules or functional groups [123–128]. Recently, Li et al. designed a nanocomposite consisting of two different layers as sandwiching ELISA-based immunosensors for detecting hepatitis B virus (HBV) antigens [87]. Basically, the first layer was the composite of porous graphene oxide/Au (pGO/Au) provided a large surface area for efficiently immobilizing antibodies (HBV antigen primary antibody (Ab₁)), fast electron transportation, and good biocompatibility [129]. The second layer was the composite of MoS₂ nanoflakes with Pt NPs and Cu₂O nanocrystals (MoS₂@Cu₂O-Pt) with HBV antigen secondary antibody (Ab₂) that showed excellent electron transfer efficiency on the electrode surface and reduction efficiency of H₂O₂ for enhancing the immunosensor sensitivity. Therefore, Ab₁-bearing pGO/Au matrix firstly captured HBV antigens, which were then sandwiched by Ab₂-bearing MoS₂@Cu₂O-Pt nanocomposites. Different concentrations of HBV antigens sandwiched by the MoS₂@Cu₂O-Pt varied the platform electrocatalytic activity degree for reducing H₂O₂ (forming H₂ and O₂) and led to the change of electronic current response. H₂O₂ reduction increased equivalent circuit resistance and lowered the transfer current. Such platform demonstrated a broad range of detection levels from 0.5 pg mL⁻¹ to 200 ng mL⁻¹, with LOD at 0.15 pg mL⁻¹ (signal-to-noise ratio of 3). A similar study by the same group replaced the second layer with the composite composed of gold@palladium nanoparticles loaded by MoS₂ functionalized multiwalled carbon nanotubes (Au@Pd/MoS₂@MWCNTs) for further improving the platform sensitivity by providing more catalytically active sites in the dendrite Au@Pd [91]. The LOD of this immunosensor for hepatitis B e antigen detection was improved to 26 fg mL⁻¹. These platforms demonstrated a novel electrochemical approach to probe viral antigens.

ZnO is also one of the biocompatible and biodegradable n-type semiconductor materials with a wide direct bandgap (3.37 eV) and large exciton binding energy (60 meV) at room temperature [130,131]. ZnO has been a critical component of gas sensors and photodetectors due to its good ability to respond to different gases [132,133]. MoS₂ nanosheets are p-type semiconductors and have a relatively narrow bandgap. A hybrid system consisting of MoS₂ and ZnO can form p–n heterojunction that permits current flow. During the COVID-19 in 2021, Shariati et al. reported a FET biosensor based on MoS₂ nanowires (NWs) mineralized with ZnO through the vapor-liquid-solid (VLS) technique to enhance the sensitivity for the detection of HBV DNA (Figure 11) [115]. The sensing principle was based on immobilized ssDNA for probing HBV DNA sequence, thereby causing the change of forwarding and backward gate-source voltage in successive sweeps. Such nanocomposite showed excellent electronic transfer characteristics with good repeatability and stability.

More importantly, the dynamic response time of the FET biosensor was 25s with LOD at 1 fM. These findings illustrated the importance of combining metal oxide nanomaterials with TMD-constructed biosensors for better FET biosensor performance.

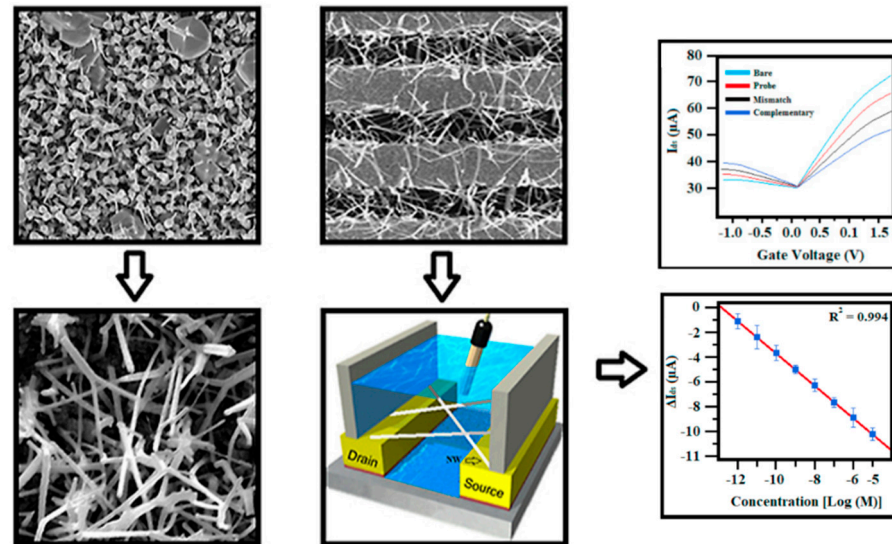


Figure 11. The morphological and crystal structure characterization of the fabricated ZnO NPs doped MoS₂ nanowires (NWs)-based FET biosensor for HBV DNA detection. The doped MoS₂ NWs device showed differential transfer characteristics for bare FET and after the immobilization of various targeting DNA sequence concentrations. The drain-source current changes showed a linear range against concentrations from 1 pM to 10 μM. The figure is adopted and reprinted with permission from Ref. [115]. Copyright Elsevier Ltd. (2021).

2.1.6. Summary

Taking advantages of the unique physical and chemical properties, 2D TMD-based nanocomposites offer a great variety of applications for sensing protein and nucleic acids through the basis of electrochemical, FET, SPR, and photoluminescence approach. Considering the current pandemic situation, the detection of SARS-CoV-2 through nucleic acids or protein entities has been growing demand for infection screening. We review recent advances of 2D TMD-based proteins/nucleic acids biosensors, emphasizing the working media and sensing mechanism. Hybrid/nanocomposites of TMDs materials with metal oxides or conductive polymers can optimize the sensitivity and device stability for detecting biomarkers.

3. Conclusions and Perspective

In the current outbreak of COVID-19, it is highly desirable to develop an efficient point-of-care residence community-level testing of SARS-CoV-2 as an initial screening of positive cases apart from conventional methods. 2D TMDs are emerging 2D nanomaterials with a wide variety of individuals offering attractive properties, including high carrier mobility, direct and tunable bandgap, and high transistor switching characteristics that are necessary as cost-effective and sensitive biosensors for probing SARS-CoV-2. The elements, polymorphs, morphologies of TMDs with the composites of other nanomaterials are taken into consideration for designing the performance of detecting various targets.

In particular, those flexible FET biosensors are highly potential as on-site biomarker detectors that are small scale, mobile, fast-response, and capable of generating readable signals (digital display) for the layman. To develop a high-performance biosensor for virus detection, integrated logic circuits can be considered for constructing a multiplexed detection of target molecules simultaneously in FET sensors [134]. Indeed, 2D TMD-based smart sensors for virus detection have been limited. The application of machine learning for 2D

TMD-based biosensors is extremely attractive to improve detection performance. Zhu and colleagues reported a platform that combined machine learning (ML) and MoS₂/MWCNTs porous nanohybrid network with oxidase-like characteristics as electrochemical nanozymes sensor to analyze carbendazim (CBZ) residues in tea and rice samples [135]. The authors utilized an artificial neural network (ANN) to learn the relationship between the processing parameters (e.g., electrochemical signals and the CBZ concentrations) to build an accurate and predictive regression model for the platform. Therefore, the readout of the platform can be more reliable using intelligent analysis. Apart from software improvement, top-gate type FET can be chosen for providing a relatively strong gate coupling and field penetration to achieve a high on/off current ratio up to 10⁵ [136]. For instance, Huang et al. showed that a top-gated FET glucose detector consisted of SnS₂, black phosphorus, and multilayered (45 nm) MoS₂ channel to withstand rapid bias changes while SiO₂ bottom-gated of the counterpart could not turn off the current of the thick MoS₂ channel effectively even with a large voltage [137]. In short, these approaches can be potentially used to develop high-performance biosensors for the virus.

Yet, most of the TMD biosensor studies remain at the laboratory stage despite their superiorities in detecting nucleic acids and proteins. High cost, poor uniformity, and difficulties of mass-production can be the main hurdles for commercializing TMD devices [58]. Overall, 2D TMD-based biosensors are a promising platform in clinical point-of-care analysis and are alternative options apart from graphene. We believe that more research will be done on this field for low-cost and large-scale fabrication and miniaturizing the microdevice to develop next-generation viral biosensors.

Author Contributions: Conceptualization, C.Y.K.L., Q.Z. and S.H.D.W.; methodology, C.Y.K.L., Q.Z. and B.Y.; data curation, Y.H. and H.W.; writing—original draft preparation, C.Y.K.L., Q.Z., B.Y. and S.H.D.W.; writing—review and editing, C.Y.K.L., B.Y., Q.Z., S.H.D.W. and M.Y.; supervision, S.H.D.W. and M.Y. All authors have read and agreed to the published version of the manuscript.

Funding: This research is funded by the Department of Biomedical Engineering of the Hong Kong Polytechnic University and grant number A0033912 and 0035876.

Acknowledgments: S.H.D.W. would like to acknowledge the Department of Biomedical Engineering of the Hong Kong Polytechnic University for supporting this work.

Conflicts of Interest: The authors declare no conflict of interest.

References

1. Bos, L. The embryonic beginning of virology: Unbiased thinking and dogmatic stagnation. *Arch. Virol.* **1995**, *140*, 613–619. [[CrossRef](#)] [[PubMed](#)]
2. Bos, L. Beijerinck's work on tobacco mosaic virus: Historical context and legacy. *Philos. Trans. R. Soc. Lond. B Biol. Sci.* **1999**, *354*, 675–685. [[CrossRef](#)] [[PubMed](#)]
3. Prangishvili, D.; Forterre, P.; Garrett, R.A. Viruses of the Archaea: A unifying view. *Nat. Rev. Microbiol.* **2006**, *4*, 837–848. [[CrossRef](#)]
4. Edwards, R.; Rohwer, F. Viral metagenomics. *Nat. Rev. Genet.* **2005**, *3*, 504–510. [[CrossRef](#)] [[PubMed](#)]
5. Geraets, J.; Dykeman, E.C.; Stockley, P.; Ranson, N.; Twarock, R. Asymmetric Genome Organization in an RNA Virus Revealed via Graph-Theoretical Analysis of Tomographic Data. *PLoS Comput. Biol.* **2015**, *11*, e1004146. [[CrossRef](#)]
6. Takizawa, T.; Matsukawa, S.; Higuchi, Y.; Nakamura, S.; Nakanishi, Y.; Fukuda, R. Induction of programmed cell death (apoptosis) by influenza virus infection in tissue culture cells. *J. Gen. Virol.* **1993**, *74*, 2347–2355. [[CrossRef](#)]
7. Zhu, Z.; Lian, X.; Su, X.; Wu, W.; Marraro, G.A.; Zeng, Y. From SARS and MERS to COVID-19: A brief summary and comparison of severe acute respiratory infections caused by three highly pathogenic human coronaviruses. *Respir. Res.* **2020**, *21*, 224. [[CrossRef](#)]
8. Yang, Y.; Peng, F.; Wang, R.; Guan, K.; Jiang, T.; Xu, G.; Sun, J.; Chang, C. The deadly coronaviruses: The 2003 SARS pandemic and the 2020 novel coronavirus epidemic in China. *J. Autoimmun.* **2020**, *109*, 102434. [[CrossRef](#)]
9. Xu, R.-H.; He, J.-F.; Evans, M.R.; Peng, G.-W.; E Field, H.; Yu, D.-W.; Lee, C.-K.; Luo, H.-M.; Lin, W.-S.; Lin, P.; et al. Epidemiologic Clues to SARS Origin in China. *Emerg. Infect. Dis.* **2004**, *10*, 1030–1037. [[CrossRef](#)]
10. Gumel, A.; Ruan, S.; Day, T.; Watmough, J.; Brauer, F.; Driessche, P.V.D.; Gabrielson, D.; Bowman, C.; Alexander, M.E.; Ardal, S.; et al. Modelling strategies for controlling SARS outbreaks. *Proc. R. Soc. B Biol. Sci.* **2004**, *271*, 2223–2232. [[CrossRef](#)] [[PubMed](#)]
11. Perlman, S.; Azhar, E.; Memish, Z.; Hui, D.S.; Zumla, P.S.A. Confronting the persisting threat of the Middle East respiratory syndrome to global health security. *Lancet Infect. Dis.* **2020**, *20*, 158–160. [[CrossRef](#)]

12. Richter, C.D. European Patent Office grants controversial patent protecting virus: Lessons from the Middle East respiratory syndrome coronavirus outbreak. *Nat. Biotechnol.* **2021**, *39*, 287–290. [[CrossRef](#)] [[PubMed](#)]
13. Wang, C.; Wang, Z.; Wang, G.; Lau, J.Y.-N.; Zhang, K.; Li, W. COVID-19 in early 2021: Current status and looking forward. *Signal. Transduct. Target. Ther.* **2021**, *6*, 1–14. [[CrossRef](#)] [[PubMed](#)]
14. Plante, J.A.; Liu, Y.; Liu, J.; Xia, H.; Johnson, B.A.; Lokugamage, K.G.; Zhang, X.; Muruato, A.E.; Zou, J.; Fontes-Garfias, C.R.; et al. Spike mutation D614G alters SARS-CoV-2 fitness. *Nature* **2021**, *592*, 116–121. [[CrossRef](#)] [[PubMed](#)]
15. Rees-Spear, C.; Muir, L.; Griffith, S.A.; Heaney, J.; Aldon, Y.; Snitselaar, J.L.; Thomas, P.; Graham, C.; Seow, J.; Lee, N.; et al. The effect of spike mutations on SARS-CoV-2 neutralization. *Cell Rep.* **2021**, *34*, 108890. [[CrossRef](#)] [[PubMed](#)]
16. Cao, J.; Li, D. Searching for human oncoviruses: Histories, challenges, and opportunities. *J. Cell. Biochem.* **2018**, *119*, 4897–4906. [[CrossRef](#)]
17. Douek, D.C.; Roederer, M.; Koup, R.A. Emerging Concepts in the Immunopathogenesis of AIDS. *Annu. Rev. Med.* **2009**, *60*, 471–484. [[CrossRef](#)]
18. Sirohi, D.; Chen, Z.; Sun, L.; Klose, T.; Pierson, T.C.; Rossmann, M.G.; Kuhn, R.J. The 3.8 Å resolution cryo-EM structure of Zika virus. *Science* **2016**, *352*, 467–470. [[CrossRef](#)]
19. Jacob, S.T.; Crozier, I.; Wahl, V.; Griffiths, A.; Bollinger, L.; Kuhn, J.H.; Fischer, W.A., II; Hewlett, A.; Kraft, C.S.; De La Vega, M.-A.; et al. Ebola virus disease. *Nat. Rev. Prim.* **2020**, *6*, 13. [[CrossRef](#)]
20. Hematian, A.; Sadeghifard, N.; Mohebi, R.; Taherikalani, M.; Nasrolahi, A.; Amraei, M.; Ghafourian, S. Traditional and Modern Cell Culture in Virus Diagnosis. *Osong Public Health Res. Perspect.* **2016**, *7*, 77–82. [[CrossRef](#)] [[PubMed](#)]
21. Nisalak, A. Laboratory diagnosis of dengue virus infections. *Southeast. Asian J. Trop. Med. Public Health* **2015**, *46*, 55–76. [[PubMed](#)]
22. Sridhar, S.; To, K.; Chan, J.F.-W.; Lau, S.K.P.; Woo, P.C.Y.; Yuen, K.-Y. A Systematic Approach to Novel Virus Discovery in Emerging Infectious Disease Outbreaks. *J. Mol. Diagn.* **2015**, *17*, 230–241. [[CrossRef](#)] [[PubMed](#)]
23. Mokhtarzadeh, A.; Eivazzadeh-Keihan, R.; Pashazadeh, P.; Hejazi, M.; Gharaatifar, N.; Hasanzadeh, M.; Baradaran, B.; de la Guardia, M. Nanomaterial-based biosensors for detection of pathogenic virus. *TrAC Trends Anal. Chem.* **2017**, *97*, 445–457. [[CrossRef](#)] [[PubMed](#)]
24. Balasuriya, U.B.R.; Crossley, B.M.; Timoney, P.J. A review of traditional and contemporary assays for direct and indirect detection of *Equid herpesvirus 1* in clinical samples. *J. Vet. Diagn. Investig.* **2015**, *27*, 673–687. [[CrossRef](#)]
25. Mathew, T. Cultivation and immunological studies of the pox group of viruses. I. Propagation of vaccinia virus in hamster kidney cell culture. *Indian J. Pathol. Bacteriol.* **1966**, *9*, 207–213. [[PubMed](#)]
26. Brumback, B.G.; Wade, C.D. Simultaneous culture for adenovirus, cytomegalovirus, and herpes simplex virus in same shell vial by using three-color fluorescence. *J. Clin. Microbiol.* **1994**, *32*, 2289–2290. [[CrossRef](#)]
27. Klespies, S.L.; E Cebula, D.; Kelley, C.L.; Galehouse, D.; Maurer, C.C. Detection of enteroviruses from clinical specimens by spin amplification shell vial culture and monoclonal antibody assay. *J. Clin. Microbiol.* **1996**, *34*, 1465–1467. [[CrossRef](#)]
28. Hsiung, G.D. Diagnostic virology: From animals to automation. *Yale J. Boil. Med.* **1984**, *57*, 727–733.
29. Hirst, G.K. The quantitative determination of influenza virus and antibodies by means of red cell agglutination. *J. Exp. Med.* **1942**, *75*, 49–64. [[CrossRef](#)]
30. Haga, T.; Nagaki, D.; Iwasaki, K. Studies on bacterial hemagglutination. II. Hemagglutination inhibiting substance of stroma. *Kitasato Arch. Exp. Med.* **1951**, *23*, 105–109.
31. Killian, M.L. Hemagglutination Assay for Influenza Virus. *Methods Mol. Biol.* **2014**, *1161*, 3–9. [[CrossRef](#)]
32. Noah, D.L.; Hill, H.; Hines, D.; White, E.L.; Wolff, M.C. Qualification of the Hemagglutination Inhibition Assay in Support of Pandemic Influenza Vaccine Licensure. *Clin. Vaccine Immunol.* **2009**, *16*, 558–566. [[CrossRef](#)]
33. Poirot, E.; Levine, M.Z.; Russell, K.; Stewart, R.J.; Pompey, J.M.; Chiu, S.; Fry, A.M.; Gross, L.; Havers, F.P.; Li, Z.-N.; et al. Detection of Avian Influenza A(H7N2) Virus Infection among Animal Shelter Workers Using a Novel Serological Approach—New York City, 2016–2017. *J. Infect. Dis.* **2019**, *219*, 1688–1696. [[CrossRef](#)]
34. Müthing, J.; Unland, F. A comparative assessment of TLC overlay technique and microwell adsorption assay in the examination of influenza A and Sendai virus specificities towards oligosaccharides and sialic acid linkages of gangliosides. *Glycoconj. J.* **1994**, *11*, 486–492. [[CrossRef](#)]
35. A Petrenko, V.; Sorokulova, I.B. Detection of biological threats. A challenge for directed molecular evolution. *J. Microbiol. Methods* **2004**, *58*, 147–168. [[CrossRef](#)]
36. Hazelton, P.R.; Gelderblom, H.R. Electron microscopy for rapid diagnosis of infectious agents in emergent situations. *Emerg. Infect. Dis.* **2003**, *9*, 294–303. [[CrossRef](#)] [[PubMed](#)]
37. Almeida, J.; Goffe, A. Antibody to wart virus in human sera demonstrated by electron microscopy and precipitin tests. *Lancet* **1965**, *286*, 1205–1207. [[CrossRef](#)]
38. Briquet, S.; Vaquero, C. Immunolocalization Studies of an Antisense Protein in HIV-1-Infected Cells and Viral Particles. *Virology* **2002**, *292*, 177–184. [[CrossRef](#)] [[PubMed](#)]
39. Fornera, S.; Walde, P. Spectrophotometric quantification of horseradish peroxidase with o-phenylenediamine. *Anal. Biochem.* **2010**, *407*, 293–295. [[CrossRef](#)] [[PubMed](#)]
40. Lagunas-Rangel, F.A.; Chavez-Valencia, V. What do we know about the antibody responses to SARS-CoV-2? *Immunobiology* **2021**, *226*, 152054. [[CrossRef](#)]

41. Dutta, N.K.; Mazumdar, K.; Gordy, J.T. The Nucleocapsid Protein of SARS-CoV-2: A Target for Vaccine Development. *J. Virol.* **2020**, *94*, e00647-20. [[CrossRef](#)]
42. Zhang, L.; Guo, H. Biomarkers of COVID-19 and technologies to combat SARS-CoV-2. *Adv. Biomark. Sci. Technol.* **2020**, *2*, 1–23. [[CrossRef](#)]
43. Jalandra, R.; Yadav, A.K.; Verma, D.; Dalal, N.; Sharma, M.; Singh, R.; Kumar, A.; Solanki, P.R. Strategies and perspectives to develop SARS-CoV-2 detection methods and diagnostics. *Biomed. Pharm.* **2020**, *129*, 110446. [[CrossRef](#)] [[PubMed](#)]
44. Helmy, Y.A.; Fawzy, M.; Elasad, A.; Sobieh, A.; Kenney, S.P.; Shehata, A.A. The COVID-19 Pandemic: A Comprehensive Review of Taxonomy, Genetics, Epidemiology, Diagnosis, Treatment, and Control. *J. Clin. Med.* **2020**, *9*, 1225. [[CrossRef](#)] [[PubMed](#)]
45. Li, D.; Zhang, J.; Li, J. Primer design for quantitative real-time PCR for the emerging Coronavirus SARS-CoV-2. *Theranostics* **2020**, *10*, 7150–7162. [[CrossRef](#)]
46. Michel, C.J.; Mayer, C.; Poch, O.; Thompson, J.D. Characterization of accessory genes in coronavirus genomes. *Virol. J.* **2020**, *17*, 131. [[CrossRef](#)] [[PubMed](#)]
47. Park, M.; Won, J.; Choi, B.Y.; Lee, C.J. Optimization of primer sets and detection protocols for SARS-CoV-2 of coronavirus disease 2019 (COVID-19) using PCR and real-time PCR. *Exp. Mol. Med.* **2020**, *52*, 963–977. [[CrossRef](#)] [[PubMed](#)]
48. Kim, S.; Lee, J.H.; Lee, S.; Shim, S.; Nguyen, T.T.; Hwang, J.; Kim, H.; Choi, Y.O.; Hong, J.; Bae, S.; et al. The Progression of SARS Coronavirus 2 (SARS-CoV2): Mutation in the Receptor Binding Domain of Spike Gene. *Immune Netw.* **2020**, *20*, e41. [[CrossRef](#)]
49. Huang, W.E.; Lim, B.; Hsu, C.C.; Xiong, D.; Wu, W.; Yu, Y.J.; Jia, H.D.; Wang, Y.; Zeng, Y.D.; Ji, M.M.; et al. RT-LAMP for rapid diagnosis of coronavirus SARS-CoV-2. *Microb. Biotechnol.* **2020**, *13*, 950–961. [[CrossRef](#)]
50. Chakraborty, D.; Kumar, S.; Chandrasekaran, N.; Mukherjee, A. Viral Diagnostics and Preventive Techniques in the Era of COVID-19: Role of Nanoparticles. *Front. Nanotechnol.* **2020**, *2*, 588795. [[CrossRef](#)]
51. Carter, L.J.; Garner, L.V.; Smoot, J.W.; Li, Y.; Zhou, Q.; Saveson, C.J.; Sasso, J.M.; Gregg, A.C.; Soares, D.J.; Beskid, T.R.; et al. Assay Techniques and Test Development for COVID-19 Diagnosis. *ACS Cent. Sci.* **2020**, *6*, 591–605. [[CrossRef](#)] [[PubMed](#)]
52. Thai, H.T.C.; Le, M.Q.; Vuong, C.D.; Parida, M.; Minekawa, H.; Notomi, T.; Hasebe, F.; Morita, K. Development and Evaluation of a Novel Loop-Mediated Isothermal Amplification Method for Rapid Detection of Severe Acute Respiratory Syndrome Coronavirus. *J. Clin. Microbiol.* **2004**, *42*, 1956–1961. [[CrossRef](#)]
53. Broughton, J.P.; Deng, X.D.; Yu, G.X.; Fasching, C.L.; Servellita, V.; Singh, J.; Miao, X.; Streithorst, J.A.; Granados, A.; Sotomayor-Gonzalez, A.; et al. CRISPR-Cas12-based detection of SARS-CoV-2. *Nat. Biotechnol.* **2020**, *38*, 870–874. [[CrossRef](#)] [[PubMed](#)]
54. Hashtroudi, H.; Mackinnon, I.D.R.; Shafiei, M. Emerging 2D hybrid nanomaterials: Towards enhanced sensitive and selective conductometric gas sensors at room temperature. *J. Mater. Chem. C* **2020**, *8*, 13108–13126. [[CrossRef](#)]
55. Gleason, A.M. Remote Monitoring of a Work-From-Home Employee to Identify Stress: A Case Report. *Work. Health Saf.* **2021**. [[CrossRef](#)] [[PubMed](#)]
56. Vermisoglou, E.; Panáček, D.; Jayaramulu, K.; Pykal, M.; Frébort, I.; Kolář, M.; Hajdúch, M.; Zbořil, R.; Otyepka, M. Human virus detection with graphene-based materials. *Biosens. Bioelectron.* **2020**, *166*, 112436. [[CrossRef](#)] [[PubMed](#)]
57. Ehtesabi, H. Application of carbon nanomaterials in human virus detection. *J. Sci. Adv. Mater. Devices* **2020**, *5*, 436–450. [[CrossRef](#)]
58. Chen, X.; Liu, C.; Mao, S. Environmental Analysis with 2D Transition-Metal Dichalcogenide-Based Field-Effect Transistors. *Nano-Micro Lett.* **2020**, *12*, 1–24. [[CrossRef](#)]
59. Kannan, P.K.; Late, D.J.; Morgan, H.; Rout, C.S. Recent developments in 2D layered inorganic nanomaterials for sensing. *Nanoscale* **2015**, *7*, 13293–13312. [[CrossRef](#)]
60. Wu, J.; Lv, W.; Yang, Q.; Li, H.; Li, F. Label-free homogeneous electrochemical detection of MicroRNA based on target-induced anti-shielding against the catalytic activity of two-dimension nanozyme. *Biosens. Bioelectron.* **2021**, *171*, 112707. [[CrossRef](#)]
61. Li, H.; Lv, W.; Yang, Q.; Li, Q.; Li, F. Inorganic Recognizer-Assisted Homogeneous Electrochemiluminescence Determination of Organophosphorus Pesticides via Target-Controlled Emitter Release. *J. Agric. Food Chem.* **2021**, *69*, 6087–6095. [[CrossRef](#)] [[PubMed](#)]
62. Wu, J.; Yang, Q.; Li, Q.; Li, H.; Li, F. Two-Dimensional MnO₂ Nanozyme-Mediated Homogeneous Electrochemical Detection of Organophosphate Pesticides without the Interference of H₂O₂ and Color. *Anal. Chem.* **2021**, *93*, 4084–4091. [[CrossRef](#)] [[PubMed](#)]
63. Védrine, J.C. Metal Oxides in Heterogeneous Oxidation Catalysis: State of the Art and Challenges for a More Sustainable World. *ChemSusChem* **2019**, *12*, 577–588. [[CrossRef](#)] [[PubMed](#)]
64. Choi, W.; Choudhary, N.; Han, G.H.; Park, J.; Akinwande, D.; Lee, Y.H. Recent development of two-dimensional transition metal dichalcogenides and their applications. *Mater. Today* **2017**, *20*, 116–130. [[CrossRef](#)]
65. Huy, V.H.; Ahn, Y.; Hur, J. Recent Advances in Transition Metal Dichalcogenide Cathode Materials for Aqueous Rechargeable Multivalent Metal-Ion Batteries. *Nanomaterials* **2021**, *11*, 1517. [[CrossRef](#)]
66. Ahmed, S.; Yi, J. Two-Dimensional Transition Metal Dichalcogenides and Their Charge Carrier Mobilities in Field-Effect Transistors. *Nano-Micro Lett.* **2017**, *9*, 1–23. [[CrossRef](#)]
67. Teo, W.Z.; Chng, E.L.K.; Sofer, Z.; Pumera, M. Cytotoxicity of Exfoliated Transition-Metal Dichalcogenides (MoS₂, WS₂, and WSe₂) is Lower Than That of Graphene and its Analogues. *Chem. A Eur. J.* **2014**, *20*, 9627–9632. [[CrossRef](#)]
68. Pessoa-Pureur, R.; Heimfarth, L.; Rocha, J.B. Signaling Mechanisms and Disrupted Cytoskeleton in the Diphenyl Ditelluride Neurotoxicity. *Oxidative Med. Cell. Longev.* **2014**, *2014*, 1–21. [[CrossRef](#)]
69. Bhanu, U.; Islam, M.R.; Tetard, L.; Khondaker, S.I. Photoluminescence quenching in gold—MoS₂ hybrid nanoflakes. *Sci. Rep.* **2014**, *4*, 5575. [[CrossRef](#)]

70. Loo, A.H.; Bonanni, A.; Pumera, M. Strong dependence of fluorescence quenching on the transition metal in layered transition metal dichalcogenide nanoflakes for nucleic acid detection. *Analyst*. **2016**, *141*, 4654–4658. [[CrossRef](#)]
71. Enyashin, A.N.; Yadgarov, L.; Houben, L.; Popov, I.; Weidenbach, M.; Tenne, R.; Bar-Sadan, M.; Seifert, G. New Route for Stabilization of 1T-WS₂ and MoS₂ Phases. *J. Phy. Chem. C* **2011**, *115*, 24586–24591. [[CrossRef](#)]
72. Lan, L.; Chen, D.; Yao, Y.; Peng, X.; Wu, J.; Li, Y.; Ping, J.; Ying, Y. Phase-Dependent Fluorescence Quenching Efficiency of MoS₂ Nanosheets and Their Applications in Multiplex Target Biosensing. *ACS Appl. Mater. Interfaces* **2018**, *10*, 42009–42017. [[CrossRef](#)] [[PubMed](#)]
73. Barua, S.; Dutta, H.S.; Gogoi, S.; Devi, R.; Khan, R. Nanostructured MoS₂-Based Advanced Biosensors: A Review. *ACS Appl. Nano Mater.* **2017**, *1*, 2–25. [[CrossRef](#)]
74. Zhao, Z.-Y.; Liu, Q.-L. Study of the layer-dependent properties of MoS₂ nanosheets with different crystal structures by DFT calculations. *Catal. Sci. Technol.* **2018**, *8*, 1867–1879. [[CrossRef](#)]
75. Fan, Q.; Wang, L.; Xu, D.; Duo, Y.; Gao, J.; Zhang, L.; Wang, X.; Chen, X.; Li, J.; Zhang, H. Solution-gated transistors of two-dimensional materials for chemical and biological sensors: Status and challenges. *Nanoscale* **2020**, *12*, 11364–11394. [[CrossRef](#)] [[PubMed](#)]
76. Wang, Y.; Xiao, J.; Zhu, H.; Li, Y.; Alsaid, Y.; Fong, K.Y.; Zhou, Y.; Wang, S.; Shi, W.; Wang, Y.; et al. Structural phase transition in monolayer MoTe₂ driven by electrostatic doping. *Nat. Cell Biol.* **2017**, *550*, 487–491. [[CrossRef](#)] [[PubMed](#)]
77. Song, S.; Keum, D.H.; Cho, S.; Perello, D.; Kim, Y.; Lee, Y.H. Room Temperature Semiconductor–Metal Transition of MoTe₂ Thin Films Engineered by Strain. *Nano Lett.* **2016**, *16*, 188–193. [[CrossRef](#)] [[PubMed](#)]
78. Sun, X.; Deng, H.; Zhu, W.; Yu, Z.; Wu, C.; Xie, Y. Interface Engineering in Two-Dimensional Heterostructures: Towards an Advanced Catalyst for Ullmann Couplings. *Angew. Chem. Int. Ed.* **2015**, *55*, 1704–1709. [[CrossRef](#)]
79. Kufer, D.; Nikitskiy, I.; Lasanta, T.; Navickaite, G.; Koppens, F.; Konstantatos, G. Hybrid 2D-0D MoS₂-PbS Quantum Dot Photodetectors. *Adv. Mater.* **2015**, *27*, 176–180. [[CrossRef](#)]
80. Patolsky, F.; Zheng, G.; Hayden, O.; Lakadamyali, M.; Zhuang, X.; Lieber, C.M. Electrical detection of single viruses. *Proc. Natl. Acad. Sci. USA* **2004**, *101*, 14017–14022. [[CrossRef](#)]
81. Mohanty, N.; Berry, V. Graphene-Based Single-Bacterium Resolution Biodevice and DNA Transistor: Interfacing Graphene Derivatives with Nanoscale and Microscale Biocomponents. *Nano Lett.* **2008**, *8*, 4469–4476. [[CrossRef](#)] [[PubMed](#)]
82. Guo, X.; Small, J.P.; Klare, J.E.; Wang, Y.; Purewal, M.S.; Tam, I.W.; Hong, B.H.; Caldwell, R.; Huang, L.; O'Brien, S.; et al. Covalently Bridging Gaps in Single-Walled Carbon Nanotubes with Conducting Molecules. *Science* **2006**, *311*, 356–359. [[CrossRef](#)] [[PubMed](#)]
83. Zhang, P.; Yang, S.; Pineda-Gomez, R.; Ibarlucea, B.; Ma, J.; Lohe, M.R.; Akbar, T.F.; Baraban, L.; Cuniberti, G.; Feng, X. Electrochemically Exfoliated High-Quality 2H-MoS₂ for Multiflake Thin Film Flexible Biosensors. *Small* **2019**, *15*, e1901265. [[CrossRef](#)]
84. Ge, J.; Ou, E.C.; Yu, R.Q.; Chu, X. A novel aptameric nanobiosensor based on the self-assembled DNA-MoS₂ nanosheet architecture for biomolecule detection. *J. Mater. Chem. B* **2014**, *2*, 625–628. [[CrossRef](#)] [[PubMed](#)]
85. Yoo, G.; Park, H.; Kim, M.; Song, W.G.; Jeong, S.; Kim, M.H.; Lee, H.; Lee, S.W.; Hong, Y.K.; Lee, M.G.; et al. Real-time electrical detection of epidermal skin MoS₂ biosensor for point-of-care diagnostics. *Nano Res.* **2017**, *10*, 767–775. [[CrossRef](#)]
86. Kukkar, M.; Tuteja, S.K.; Sharma, A.L.; Kumar, V.; Paul, A.K.; Kim, K.-H.; Sabherwal, P.; Deep, A. A New Electrolytic Synthesis Method for Few-Layered MoS₂ Nanosheets and Their Robust Biointerfacing with Reduced Antibodies. *ACS Appl. Mater. Interfaces* **2016**, *8*, 16555–16563. [[CrossRef](#)] [[PubMed](#)]
87. Park, H.; Lee, H.; Jeong, S.H.; Lee, E.; Lee, W.; Liu, N.; Yoon, D.S.; Kim, S.; Lee, S.W. MoS₂ Field-Effect Transistor-Amyloid-beta1-42 Hybrid Device for Signal Amplified Detection of MMP-9. *Anal. Chem.* **2019**, *91*, 8252–8258. [[CrossRef](#)] [[PubMed](#)]
88. Shi, J.; Lyu, J.; Tian, F.; Yang, M. A fluorescence turn-on biosensor based on graphene quantum dots (GQDs) and molybdenum disulfide (MoS₂) nanosheets for epithelial cell adhesion molecule (EpCAM) detection. *Biosens. Bioelectron.* **2017**, *93*, 182–188. [[CrossRef](#)]
89. Shin, M.; Yoon, J.; Yi, C.; Lee, T.; Choi, J.-W. Flexible HIV-1 Biosensor Based on the Au/MoS₂ Nanoparticles/Au Nanolayer on the PET Substrate. *Nanomaterials* **2019**, *9*, 1076. [[CrossRef](#)]
90. Li, F.; Li, Y.; Feng, J.; Gao, Z.; Lv, H.; Ren, X.; Wei, Q. Facile synthesis of MoS₂@Cu₂O-Pt nanohybrid as enzyme-mimetic label for the detection of the Hepatitis B surface antigen. *Biosens. Bioelectron.* **2018**, *100*, 512–518. [[CrossRef](#)]
91. Gao, Z.; Li, Y.; Zhang, X.; Feng, J.; Kong, L.; Wang, P.; Chen, Z.; Dong, Y.; Wei, Q. Ultrasensitive electrochemical immunosensor for quantitative detection of HBeAg using Au@Pd/MoS₂@MWCNTs nanocomposite as enzyme-mimetic labels. *Biosens. Bioelectron.* **2018**, *102*, 189–195. [[CrossRef](#)] [[PubMed](#)]
92. Pathania, P.K.; Saini, J.K.; Vij, S.; Tewari, R.; Sabherwal, P.; Rishi, P.; Suri, C.R. Aptamer functionalized MoS₂-rGO nanocomposite based biosensor for the detection of Vi antigen. *Biosens. Bioelectron.* **2018**, *122*, 121–126. [[CrossRef](#)]
93. Solanki, S.; Soni, A.; Pandey, M.K.; Biradar, A.; Sumana, G. Langmuir-Blodgett Nanoassemblies of the MoS₂-Au Composite at the Air-Water Interface for Dengue Detection. *ACS Appl. Mater. Interfaces* **2018**, *10*, 3020–3028. [[CrossRef](#)] [[PubMed](#)]
94. Le, S.T.; Guros, N.B.; Bruce, R.C.; Cardone, A.; Amin, N.D.; Zhang, S.; Klauda, J.B.; Pant, H.C.; Richter, C.A.; Balijepalli, A. Quantum capacitance-limited MoS₂ biosensors enable remote label-free enzyme measurements. *Nanoscale* **2019**, *11*, 15622–15632. [[CrossRef](#)]
95. Song, Y.J.; Cao, K.H.; Li, W.J.; Ma, C.Y.; Qiao, X.W.; Li, H.L.; Hong, C.L. Optimal film thickness of rGO/MoS₂ @ polyaniline nanosheets of 3D arrays for carcinoembryonic antigen high sensitivity detection. *Microchem. J.* **2020**, *155*, 104694. [[CrossRef](#)]

96. Peng, X.; Zhou, Y.X.; Nie, K.X.; Zhou, F.F.; Yuan, Y.F.; Song, J.; Qu, J.L. Promising near-infrared plasmonic biosensor employed for specific detection of SARS-CoV-2 and its spike glycoprotein. *New J. Phys.* **2020**, *22*, 103046. [[CrossRef](#)]
97. Vasudevan, M.; Tai, M.J.Y.; Perumal, V.; Gopinath, S.C.B.; Murthe, S.S.; Ovinis, M.; Mohamed, N.M.; Joshi, N. Cellulose acetate-MoS₂ nanopetal hybrid: A highly sensitive and selective electrochemical aptasensor of Troponin I for the early diagnosis of Acute Myocardial Infarction. *J. Taiwan Inst. Chem. Eng.* **2021**, *118*, 245–253. [[CrossRef](#)]
98. Zhang, X.; Lai, Z.C.; Tan, C.L.; Zhang, H. Solution-Processed Two-Dimensional MoS₂ Nanosheets: Preparation, Hybridization, and Applications. *Angew. Chem. Int. Ed. Engl.* **2016**, *55*, 8816–8838. [[CrossRef](#)] [[PubMed](#)]
99. Zeng, Z.; Yin, Z.; Huang, X.; Li, H.; He, Q.; Lu, G.; Boey, F.; Zhang, H. Single-Layer Semiconducting Nanosheets: High-Yield Preparation and Device Fabrication. *Angew. Chem. Int. Ed.* **2011**, *50*, 11093–11097. [[CrossRef](#)]
100. Coleman, J.N.; Lotya, M.; O'Neill, A.; Bergin, S.D.; King, P.J.; Khan, U.; Young, K.; Gaucher, A.; De, S.; Smith, R.J.; et al. Two-Dimensional Nanosheets Produced by Liquid Exfoliation of Layered Materials. *Science* **2011**, *331*, 568–571. [[CrossRef](#)]
101. Navani, N.K.; Mok, W.K.; Yingfu, L. In Vitro Selection of Protein-Binding DNA Aptamers as Ligands for Biosensing Applications. *Methods Mol. Biol.* **2009**, *504*, 399–415. [[CrossRef](#)] [[PubMed](#)]
102. Johansson, M.K. Choosing Reporter-Quencher Pairs for Efficient Quenching Through Formation of Intramolecular Dimers. *Fluoresc. Energy Transf. Nucleic Acid Probes* **2006**, *335*, 17–30. [[CrossRef](#)]
103. Wong, W.K.; Wong, S.H.D.; Bian, L. Long-Term Detection of Oncogenic MicroRNA in Living Human Cancer Cells by Gold@ Polydopamine-Shell Nanoprobe. *ACS Biomater. Sci. Eng.* **2020**, *6*, 3778–3783. [[CrossRef](#)] [[PubMed](#)]
104. Lu, C.; Liu, Y.; Ying, Y.; Liu, J. Comparison of MoS₂, WS₂, and Graphene Oxide for DNA Adsorption and Sensing. *Langmuir* **2017**, *33*, 630–637. [[CrossRef](#)]
105. Wang, L.; Dong, L.; Liu, G.; Shen, X.; Wang, J.; Zhu, C.; Ding, M.; Wen, Y. Fluorometric determination of HIV DNA using molybdenum disulfide nanosheets and exonuclease III-assisted amplification. *Microchim. Acta* **2019**, *186*, 286. [[CrossRef](#)] [[PubMed](#)]
106. Zhang, Y.; Zheng, B.; Zhu, C.; Zhang, X.; Tan, C.; Li, H.; Chen, B.; Yang, J.; Chen, J.; Wang, L.; et al. Single-Layer Transition Metal Dichalcogenide Nanosheet-Based Nanosensors for Rapid, Sensitive, and Multiplexed Detection of DNA. *Adv. Mater.* **2015**, *27*, 935–939. [[CrossRef](#)]
107. Singhal, C.; Khanuja, M.; Chaudhary, N.; Pundir, C.S.; Narang, J. Detection of chikungunya virus DNA using two-dimensional MoS₂ nanosheets based disposable biosensor. *Sci. Rep.* **2018**, *8*, 7734. [[CrossRef](#)]
108. Huang, M.-B.; Xia, M.; Gao, Z.; Zhou, H.; Liu, M.; Huang, S.; Zhen, R.; Wu, J.Y.; Roth, W.W.; Bond, V.C.; et al. Characterization of Exosomes in Plasma of Patients with Breast, Ovarian, Prostate, Hepatic, Gastric, Colon, and Pancreatic Cancers. *J. Cancer Ther.* **2019**, *10*, 382–399. [[CrossRef](#)]
109. Zhang, F.; Wang, S.; Feng, J.; Zou, R.; Xiang, L.; Cai, C. MoS₂-loaded G-quadruplex molecular beacon probes for versatile detection of MicroRNA through hybridization chain reaction signal amplification. *Talanta* **2019**, *202*, 342–348. [[CrossRef](#)] [[PubMed](#)]
110. Yang, T.; Meng, L.; Chen, H.; Luo, S.; Li, W.; Jiao, K. Synthesis of Thin-Layered Molybdenum Disulfide-Based Polyaniline Nanointerfaces for Enhanced Direct Electrochemical DNA Detection. *Adv. Mater. Interfaces* **2016**, *3*, 1500700. [[CrossRef](#)]
111. Dutta, S.; Chowdhury, A.D.; Biswas, S.; Park, E.Y.; Agnihotri, N.; De, A.; De, S. Development of an effective electrochemical platform for highly sensitive DNA detection using MoS₂-Polyaniline nanocomposites. *Biochem. Eng. J.* **2018**, *140*, 130–139. [[CrossRef](#)]
112. Wang, T.; Zhu, R.; Zhuo, J.; Zhu, Z.; Shao, Y.; Li, M. Direct Detection of DNA below ppb Level Based on Thionin-Functionalized Layered MoS₂ Electrochemical Sensors. *Anal. Chem.* **2014**, *86*, 12064–12069. [[CrossRef](#)]
113. Loan, P.T.K.; Zhang, W.; Lin, C.-T.; Wei, K.-H.; Li, L.-J.; Chen, C.-H. Graphene/MoS₂ Heterostructures for Ultrasensitive Detection of DNA Hybridisation. *Adv. Mater.* **2014**, *26*, 4838–4844. [[CrossRef](#)]
114. Oudeng, G.; Benz, M.; Popova, A.A.; Zhang, Y.; Yi, C.; Levkin, P.A.; Yang, M. Droplet Microarray Based on Nanosensing Probe Patterns for Simultaneous Detection of Multiple HIV Retroviral Nucleic Acids. *ACS Appl. Mater. Interfaces* **2020**, *12*, 55614–55623. [[CrossRef](#)]
115. Shariati, M.; Vaezjalali, M.; Sadeghi, M. Ultrasensitive and easily reproducible biosensor based on novel doped MoS₂ nanowires field-effect transistor in label-free approach for detection of hepatitis B virus in blood serum. *Anal. Chim. Acta* **2021**, *1156*, 338360. [[CrossRef](#)] [[PubMed](#)]
116. Martínez-Periñán, E.; García-Mendiola, T.; Enebral-Romero, E.; del Caño, R.; Vera-Hidalgo, M.; Sulleiro, M.V.; Navío, C.; Pariente, F.; Pérez, E.M.; Lorenzo, E. A MoS₂ platform and thionine-carbon nanodots for sensitive and selective detection of pathogens. *Biosens. Bioelectron.* **2021**, *189*, 113375. [[CrossRef](#)] [[PubMed](#)]
117. Feng, T.; Chen, X.; Qiao, X.; Sun, Z.; Wang, H.; Qi, Y.; Hong, C. Graphene oxide supported rhombic dodecahedral Cu₂O nanocrystals for the detection of carcinoembryonic antigen. *Anal. Biochem.* **2016**, *494*, 101–107. [[CrossRef](#)] [[PubMed](#)]
118. Cho, I.-H.; Lee, J.; Kim, J.; Kang, M.-S.; Paik, J.K.; Ku, S.; Cho, H.-M.; Irudayaraj, J.; Kim, D.-H. Current Technologies of Electrochemical Immunosensors: Perspective on Signal Amplification. *Sensors* **2018**, *18*, 207. [[CrossRef](#)] [[PubMed](#)]
119. Yin, B.; Wu, Y.; Ma, H.; Ma, X.; Fu, B.; Liu, J. Studies on the Asymmetric Catalytic Friedel-Crafts Alkylation of Indoles with Trifluoromethyl Pyruvate Catalyzed by Heteroarylidene-BOX-Cu Complexes. *Chin. J. Org. Chem.* **2015**, *35*, 2119–2124. [[CrossRef](#)]
120. Wu, D.; Ma, H.; Zhang, Y.; Jia, H.; Yan, T.; Wei, Q. Corallite-like Magnetic Fe₃O₄@MnO₂@Pt Nanocomposites as Multiple Signal Amplifiers for the Detection of Carcinoembryonic Antigen. *ACS Appl. Mater. Interfaces* **2015**, *7*, 18786–18793. [[CrossRef](#)] [[PubMed](#)]

121. Huang, C.-L.; Weng, W.-L.; Huang, Y.-S.; Liao, C.-N. Enhanced photolysis stability of Cu₂O grown on Cu nanowires with nanoscale twin boundaries. *Nanoscale* **2019**, *11*, 13709–13713. [[CrossRef](#)] [[PubMed](#)]
122. Choi, J.W.; Yoon, J.; Lim, J.; Shin, M.; Lee, S.N. Graphene/MoS₂ Nanohybrid for Biosensors. *Materials* **2021**, *14*, 518.
123. Yin, B.; Ho, L.W.C.; Liu, S.; Hong, H.; Tian, X.Y.; Li, H.; Choi, C.H.J. Sub-10 nm Substrate Roughness Promotes the Cellular Uptake of Nanoparticles by Upregulating Endocytosis-Related Genes. *Nano Lett.* **2021**, *21*, 1839–1847. [[CrossRef](#)] [[PubMed](#)]
124. Ho, L.W.C.; Yin, B.; Dai, G.; Choi, C.H.J. Effect of Surface Modification with Hydrocarbyl Groups on the Exocytosis of Nanoparticles. *Biochemistry* **2020**, *60*, 1019–1030. [[CrossRef](#)] [[PubMed](#)]
125. Yang, H.; Yao, Y.; Li, H.; Ho, L.W.C.; Yin, B.; Yung, W.-Y.; Leung, K.C.-F.; Mak, A.F.-T.; Choi, C.H.J. Promoting intracellular delivery of sub-25 nm nanoparticles via defined levels of compression. *Nanoscale* **2018**, *10*, 15090–15102. [[CrossRef](#)]
126. Wong, S.H.D.; Yin, B.; Yang, B.; Lin, S.; Li, R.; Feng, Q.; Yang, H.; Zhang, L.; Yang, Z.; Li, G.; et al. Anisotropic Nanoscale Presentation of Cell Adhesion Ligand Enhances the Recruitment of Diverse Integrins in Adhesion Structures and Mechanosensing-Dependent Differentiation of Stem Cells. *Adv. Funct. Mater.* **2019**, *29*, 1806822. [[CrossRef](#)]
127. Yin, B.; Chan, C.K.W.; Liu, S.; Hong, H.; Wong, S.H.D.; Lee, L.K.C.; Ho, L.W.C.; Zhang, L.; Leung, K.C.-F.; Choi, P.C.-L.; et al. Intrapulmonary Cellular-Level Distribution of Inhaled Nanoparticles with Defined Functional Groups and Its Correlations with Protein Corona and Inflammatory Response. *ACS Nano* **2019**, *13*, 14048–14069. [[CrossRef](#)] [[PubMed](#)]
128. Kang, H.; Wong, S.H.D.; Pan, Q.; Li, G.; Bian, L. Anisotropic Ligand Nanogeometry Modulates the Adhesion and Polarization State of Macrophages. *Nano Lett.* **2019**, *19*, 1963–1975. [[CrossRef](#)]
129. Bei, H.P.; Yang, Y.; Zhang, Q.; Tian, Y.; Luo, X.; Yang, M.; Zhao, X. Graphene-Based Nanocomposites for Neural Tissue Engineering. *Molecules* **2019**, *24*, 658. [[CrossRef](#)] [[PubMed](#)]
130. Ni, Y.; Zhu, J.; Zhang, L.; Hong, J. Hierarchical ZnO micro/nanoarchitectures: Hydrothermal preparation, characterization and application in the detection of hydrazine. *CrystEngComm* **2010**, *12*, 2213–2218. [[CrossRef](#)]
131. Zhou, J.; Xu, N.S.; Wang, Z.L. Dissolving Behavior and Stability of ZnO Wires in Biofluids: A Study on Biodegradability and Biocompatibility of ZnO Nanostructures. *Adv. Mater.* **2006**, *18*, 2432–2435. [[CrossRef](#)]
132. Guo, J.; Peng, C. Synthesis of ZnO nanoparticles with a novel combustion method and their C₂H₅OH gas sensing properties. *Ceram. Int.* **2015**, *41*, 2180–2186. [[CrossRef](#)]
133. Fan, F.; Tang, P.; Wang, Y.; Feng, Y.; Chen, A.; Luo, R.; Li, D. Facile synthesis and gas sensing properties of tubular hierarchical ZnO self-assembled by porous nanosheets. *Sens. Actuators B Chem.* **2015**, *215*, 231–240. [[CrossRef](#)]
134. Shinde, S.M.; Das, T.; Hoang, A.T.; Sharma, B.K.; Chen, X.; Ahn, J.-H. Surface-Functionalization-Mediated Direct Transfer of Molybdenum Disulfide for Large-Area Flexible Devices. *Adv. Funct. Mater.* **2018**, *28*, 1706231. [[CrossRef](#)]
135. Zhu, X.; Liu, P.; Ge, Y.; Wu, R.; Xue, T.; Sheng, Y.; Ai, S.; Tang, K.; Wen, Y. MoS₂/MWCNTs porous nanohybrid network with oxidase-like characteristic as electrochemical nanozyme sensor coupled with machine learning for intelligent analysis of carbendazim. *J. Electroanal. Chem.* **2020**, *862*, 113940. [[CrossRef](#)]
136. Kwon, H.-J.; Kim, S.; Jang, J.; Grigoropoulos, C. Evaluation of pulsed laser annealing for flexible multilayer MoS₂ transistors. *Appl. Phys. Lett.* **2015**, *106*, 113111. [[CrossRef](#)]
137. Huang, Y.; Sutter, E.; Wu, L.M.; Xu, H.; Bao, L.; Gao, H.-J.; Zhou, X.-J.; Sutter, P. Thick Layered Semiconductor Devices with Water Top-Gates: High On–Off Ratio Field-Effect Transistors and Aqueous Sensors. *ACS Appl. Mater. Interfaces* **2018**, *10*, 23198–23207. [[CrossRef](#)] [[PubMed](#)]